Theoretical Study on the Band Structure of $Bi_{1-x}Sb_x$ Thin Films

by

Shuang Tang

Bachelor of Science, Fudan University (2009)

Submitted to the Department of Materials Science and Engineering
in partial fulfillment of the requirements for the degree of

Master of Science

at the

MASSACHUSETTS INSTITUTE OF TECHNOLOGY

June 2012

Author .....
Department of Materials Science and Engineering
February 23, 2012

Certified by .....
Mildred S. Dresselhaus
Institute Professor of Electrical Engineering and Physics
Thesis Supervisor

Certified by .....
Silvija Gradečak
Assistant Professor of Materials Science and Engineering
Thesis Reader

Accepted by .....
Gerbrand Ceder
Chairman, Departmental Committee on Graduate Students

Theoretical Study on the Band Structure of $Bi_{1-x}Sb_x$ Thin Films

by

Shuang Tang

Submitted to the Department of Materials Science and Engineering
on February 23, 2012, in partial fulfillment of the
requirements for the degree of
Master of Science

Abstract

The study on the electronic band structures of $Bi_{1-x}Sb_x$ thin films is a very interesting topic. Recall that in bulk $Bi_{1-x}Sb_x$, the electronic band structure can be varied as a function of temperature T, pressure P and stoichiometry. The electronic band structure does not change with T significantly in the cryogenic temperature range under the atmospherical presure. The conduction band edge and the valence band edge are very close to each other at the three L points within the first Brillouin zone such that they are strongly coupled, and the energy band at the L points is non-parabolic dispersive. At certain conditions, the conduction band edge and the valence band edge will touch each other at the three L points, and the dispersion relation at the L points will become linear, which leads to the formation of three-dimensional Dirac points. By synthesizing $Bi_{1-x}Sb_x$ thin films, we have two more parameters to control the band structure, namely film thickness and growth orientation.

We have developed the iterative-two-dimensional-two-band model to study the two-dimensional L-point non-parabolically dispersive electronic band structure of the $Bi_{1-x}Sb_x$ thin films system. The Lax model based on the $\mathbf{k}\cdot\mathbf{p}$ model describes the the L-point non-parabolic dispersion relations very well consistent with experimental results for bulk bismuth. Because the band gap is narrow, the number of bands that are needed in the perturbation is small. A satisfactory representation over a limited region of $\mathbf{k}$-space has been archived in terms of the two coupled bands, which means that the Hamiltonian could be approximately diagonalized, and which gives a very simple form for the Lax model. In the thin films system, the anylysis is more different due to the non-parabolic quantum confinement effect. The L-point band gap is increased in a thin film compared to the L-point band gap in a bulk system. As the film thickness decreases, the L-point band gap increases. The L-point band gap and the L-point inverse-effective-mass tensor are coupled together and are different from the values for the bulk materials. Thus, iterative procedures are employed for getting the accurate values of the L-point band gap and its corresponding inverse-effective-mass tensor. The iterative-two-dimensional-two-band model can be generalized to study other two-dimensional narrow-gap systems, for example lead telluride thin films and silicon-germanium alloys thin films. The model can also be modified to study one-dimensional narrow-gap systems such as $Bi_{1-x}Sb_x$ nanowires.

The electronic band structure of $Bi_{1-x}Sb_x$ thin films for different growth orientations

are studied. The results shows that by growing the $Bi_{1-x}Sb_x$ thin film normal to a low symmetry crystalline direction other than the trigonal axis, the three-fold symmetry of the three L points in the bulk $Bi_{1-x}Sb_x$ can be broken. Specifically, by growing the $Bi_{1-x}Sb_x$ thin film along the bisectrix axis, anisotropic single-Dirac-cone can be constructed at the L point associated with this bisectrix axis.

In similar ways, by choosing proper antimony compositions, growth orientations and film thicknesses, a large variety of Dirac-cone materials can be constructed based on the $Bi_{1-x}Sb_x$ thin films system, including single-Dirac-cone materials with different aisotropies, bi-Dirac-cone materials, tri-Dirac-cone materials, quasi-Dirac-cone materials and semi-Dirac-cone materials.

Thesis Supervisor: Mildred S. Dresselhaus
Title: Institute Professor of Electrical Engineering and Physics

Acknowledgments

I thank Prof. Mildred S. Dresselhaus for advising me through all the time in Massachusetts Institute of Technology. I also thank Prof. Gang Chen and Gene F. Dresselhaus for co-advising. Prof. Mildred Dresselhaus gave me a flexible time to search around within the groups to find out the project that I am most interested in. This is very important to me to start this $Bi_{1-x}Sb_x$ thin films project. Prof. Mildred S. Dresselhaus not only advises me on science and engineering, but also has taught me a lot about social and historical knowledge. For example, Millie often told me many interesting stories about her advisors, like Prof. Enrico Fermi, Prof. Richard Feynman and Prof. Edward Teller, about her work colleagues like Prof. Chien-Shiung Wu, about how she worked for President Bill Clinton, about her efforts on women science activities, about how she helped young faculties like Prof. Charles Lieber, about how she helped Chinese universities to build up research centers in the mid of 1980's on invitation from Chinese scientists like Prof. Xide Xie, and about how she loves her music world. Millie and Gene invited me to her family on thanks-giving day every year and let me feel warm in this country. Prof. Gang Chen often uses his stories to encourage us too, about how he became Chancellor Chang-Lin Tien's student, how he met Prof. Mildred Dresselhaus, and how he has built his success in this field step by step through hard working.

One of the many things that I respect Prof. Mildred Dresselhaus very much is that she never cares about how to be famous though she becomes superbly famous ultimately. She just does science and never cares about the trivial things like citation factors or Nobel Prizes. Millie told me she never knows why people pursue high citation factors. She suggested the Nobel committee to give the 2010 Physics Prize on graphene to young scientists even though people call her "Mother of Carbon". She never cares about being famous, but she becomes one of the most famous scientists in the world. She is the Institute Professor of MIT. She served as President of the American Society of Physics, President of the Government Consulting Group, President of the American Association for the Advancement of Science, Science Office Director of the Department of Energy etc. APS will hang out four figures in annual meetings, Richard Feynman, Marie Curie, James Maxwell, and Mildred

Dresselhaus.

I thank the help from all the professors and friends here who give me spiritual and academical supports in the family of MIT. I thank Ms. Laura Doughty and Mr. Read Schusky for all the administration processing and paperwork. I thank the discussion with Prof. Dr. Zhifeng Ren, Dr. Xiaoting Jia, Prof. Joseph Heremans, Prof. Dr. Keivan Esfarjani, Prof. Dr. Jing Kong, Prof. Dr. Elena I. Rogacheva, Dr. Dar'ya S. Orlova, Prof. Dr. Oded Rabin, Dr. Yu-Ming Lin, Dr. Mario Hofmann, Prof. Dr. Yah-Ping Hsieh, Dr. Mona Zebarjadi, Prof. Dr. Tengfei Luo, Prof. Dr. Qing Hao, Dr. Yiqun Zhang, Mr. Andrei J. Levin, Dr. Shuo Chen, Dr. Andrew Muto, Prof. Dr. Junichiro Shiomi, Dr. Jae Sik Jin, Ms. Zhiting Tian, Prof. Dr. Sheng Shen, Mr. Thomas Hirschmann, Dr. Paulo Antonio Trindade Araujo, Dr. Federico Villalpando Paez, Dr. Hootan Farhat. Dr. Ling Lu, Prof. Dr. Chuang Deng. Dr. Alfonso R. Reina Cecco, Prof. Dr. Riichiro Saito and Dr. Nicola Bonini.

I thank Dr. Yu Albert Bai, Dr. Xiaoting Jia and Mr. Feng Gao for helping me and taking care of my daily life.

I thank Prof. Zuimin Jiang, Prof. Jiyao Chen and Prof. Shihong Ma in Fudan University for recommending me to MIT.

Most importantly, I thank my father Gongming Tang and my mother Shuiqing Deng for raising me and educating me through all the years. I thank my paternal grandmother Suqing Gu. This thesis is also for the memory for my beloved grandparents, Siqun Li, Changming Xiao, Qingyun Tang, Dagui Deng.

謹以此文獻與
唐恭明
鄧水清
古素清
以誌生養之澤椿萱並茂蘭桂騰芳
謹以此文紀念
顯外祖妣李氏諱素瓊老孺人
顯外祖考肖公諱長明老大人
顯祖考唐公諱清雲老大人
顯外祖考鄧公諱大貴老大人
顯曾祖考唐公諱中華老大人
顯曾祖妣唐門毛氏老孺人
顯高祖考唐公諱安邦老大人
顯外曾祖考鄧公諱光舉老大人
顯外曾祖妣鄧門吳氏老孺人
顯外高祖考鄧公諱學泉老大人
永留誌紀
金爐不斷千秋火玉盞長明萬歲燈
尚饗

唐爽

Contents

List of Figures

List of Tables

Chapter 1

Introduction

1.1 Background

Nano-science and nano-technology have been one of the most interesting topics for the last decades. The physics of materials on the nano-scale are different from those on the marcro-scale, including electronics, magnetics and mechanics, especially when the size of the materials is reduced to a scale that is compatible with the de Broglie wavelength of the electrons. The new phenomena in nano-scale materials are due to the quantum confinment effect that can be described by quantum mechanics, which has opened a brand-new way for science research and technology applications. Novel devices can be designed based on the nano-science and nano-technology.

In the modern electronic industry, the scale of the electronic devices is shrinking in an exponential way every year. The multiple nano-devices based on thin films have been dominant for the last decade. Thus, the research and the development of thin film science and engineering are becoming more and more important.

1.2 Motivation for Studying the Electronic Band Structures of $Bi_{1-x}Sb_x$ Thin Films

Recently, bismuth-antimony alloys have been receiving particular attention from researchers, because this materials system has a number of unique physical properties that can be interesting for both fundamental studies and engineering applications. $Bi_{1-x}Sb_x$ has traditionally been considered as a promising materials system for thermoelectric and thermomagnetoelectric applications for temperatures below 200 K, especially in the design of refrigeration devices [2, 3, 4]. The band structure of $Bi_{1-x}Sb_x$ is sensitive to many parameters, such as antimony composition x [5, 6], pressure P [7, 8], external magnetic field B [9, 10, 11, 12], and temperature T [13]. $Bi_{1-x}Sb_x$ alloys can also be potentially used to design detectors for pressure measurements and mV-meters. Solid $Bi_{1-x}Sb_x$ alloys can also be found in different phases, including a gapless phase where the non-parabolic electronic dispersion relation makes a Dirac point at the L point [7, 14, 1, 15, 16, 17]. This state is of special significance to scientific researchers working on various quantum properties, such as the quantum Hall effect, the behaviors of relativistic fermions and so on. The small effective carrier masses and the high mobilities of carriers under certain conditions has also made the $Bi_{1-x}Sb_x$ a candidate for quantum computation [18, 19]. Recently, many studies have been carried out on the properties of the Dirac cone and of the photon-like fermions in few-layer graphene systems [20, 21, 22, 23, 24]. Similar studies may also be carried out for $Bi_{1-x}Sb_x$ alloys systems that are near the region of the gapless Dirac-point state.

The electronic band structure of bulk $Bi_{1-x}Sb_x$ has been widely studied. Jain et al. examined the temperature dependence of the band structure in the range of 4.2-300 K [13]. Golin et al. later proposed an empirical model for the relative energies of the band branches at some of the high symmetry points for bulk $Bi_{1-x}Sb_x$ [6]. Subsequently, the thermoelectric properties of the bulk alloys have been studied [2, 25, 26]. In 1993, Hicks and Dresselhaus suggested that low-dimensional materials could have a remarkably enhanced figure of merit ZT [27, 28], and since that time many researchers have moved in this direction. Thermoelectric properties of $Bi_{1-x}Sb_x$ nanowires have been studied by Dresselhaus and other co-workers [29, 30, 31, 32]. So far, it has been found that we can control the band struc-

tures of $Bi_{1-x}Sb_x$ nanowires through both the composition of the alloy, and the radius of the nanowires [29, 31, 33, 34, 35]. The phase diagram for $Bi_{1-x}Sb_x$ nanowires grown along the trigonal axis has been predicted [30]. However, neither theoretical nor experimental work has yet been done systematically in describing the two-dimensional electronic band structure for a $Bi_{1-x}Sb_x$ thin film as a function of the crystallographic parameters, such as film thickness and growth orientation. Recently, a phase transition to a near-gapless state, which implies a Dirac cone for the functional form of the electronic dispersion relation of carriers in bulk $Bi_{1-x}Sb_x$, has been observed [18]. However, making a gapless state and observing Dirac fermions in low-dimensional $Bi_{1-x}Sb_x$ systems is still a challenge of current interest.

1.3 Thesis Outline

In Chapter 2, the electronic band structure and the crystal structure of $Bi_{1-x}Sb_x$ alloys will be introduced, and the original Lax model for studying the non-parabolic dispersion relation at the L points of bulk bismuth will be reviewed. The iterative-two-dimensional-two-band model will be then developed, which is our basic methodology for this thesis.

Chapter 3 shows how to construct anisotropic single-Dirac-cones in the $Bi_{1-x}Sb_x$ thin film system, based on the iterative-two-dimensional-two-band model that is developed in Chapter 2, The anisotropy, the linear $E(\mathbf{k})$ and the massive fermion group velocity $\mathbf{v}(\mathbf{k})$ will be discussed.

Chapter 4 further extends the topic of constructing Dirac-cone materials. It is shown how to construct a large variety of Dirac-cone materials, including single-Dirac-cone materials, bi-Dirac-cone materials, tri-Dirac-cone materials, quasi-Dirac-cone materials and semi-Dirac-cone materials.

Lastly, the conclusions of this thesis and the future research suggestions are presented in Chapter 5.

Chapter 2

The Development of the Iterative-Two-Dimensional-Two-Band Model for the 2D $Bi_{1-x}Sb_x$ Thin Film System

2.1 Introduction

The electronic band structure of $Bi_{1-x}Sb_x$ is of special interest, and is more complicated than normal semiconductors for analysis. For bulk $Bi_{1-x}Sb_x$, there are multiple kinds of carrier pockets in its first Brillouin zone at the T point, the three L points and the six H points. The conduction band and the valence band are so close to each other in energy at the L points that they are strongly coupled. Therefore, the dispersion relations at the L points are non-parabolical due to the strong inter-band coupling. In the limit of band touching, the band structure becomes linearly dispersive at the L points, which leads to the formation of Dirac points. Lax et al. have proposed the two-band model for bulk bismuth, which describes the non-parabolic dispersion relations at the three-fold symmetric L points for pure bulk bismuth [36, 37]. In this chapter, we have developed an iterative-two-dimensional-two-band model to study the two-dimensional non-parabolic dispersion relations at the L

points for the $Bi_{1-x}Sb_x$ thin films starting from the original Lax model. The iterative-two-dimensional-two-band model I have developed will be also valid for other low-dimensional non-parabolic dispersive electronic band structures. In this chapter, I first review the crystal structure and the electronic band structure of bulk $Bi_{1-x}Sb_x$, and then review the Lax model for bulk Bi, and thereafter describe how the iterative-two-dimensional-two-band model is developed.

2.2 The Crystal Structure and the Electronic Band Structure of Bulk Bismuth-Antimony Alloys

The elements of both bismuth and antimony are in Column VI of the periodic table. The crystal structure of pure bismuth, pure antimony and their alloys is rhombohedral, which has an $R\bar{3}m$ space group symmetry [38]. There are two atoms in each unit cell of the lattice. This lattice structure can be seen as two distorted face centered cubic (FCC) sub-lattices inter-penetrating together, where each of the FCC sub-lattices is elonged along the trigonal axis and the two sub-lattices are displayed along the same trigonal axis, as shown in Fig. 2-1. A natural Cartesian coordinate system is defined by this rhombohedral structure. The trigonal axis with C_3 symmetry is the Z-axis denoted as $[001]$, the binary axis with C_2 symmetry is the X-axis denoted as $[100]$, and the bisectrix axis, which is perpendicular to both the trigonal axis and the binary axis, is the Y-axis denoted as $[100]$. Because of the C_3 symmetry of the trigonal axis, it is also common for researchers to use a hexagonal notation to describe different crystalline directions, where the trigonal axis, the binary axis and the bisectrix axis are denoted, respectively, by $[0001]$ $[1\bar{2}10]$ and $[10\bar{1}0]$, as shown in Fig. 2-2. The lattice parameters of bulk $Bi_{1-x}Sb_x$ change monotonically with antimony composition x [13]. In terms of the hexagonal cell lattice parameters, a changes linearly with antimony composition x and obeys the Vegard's Law. However, the change of lattice parameter c as a function of antimony composition x deviates from the Vegard's Law. The lattice parameters for pure bulk bismuth and pure bulk antimony used in this thesis are listed in Table 2.1

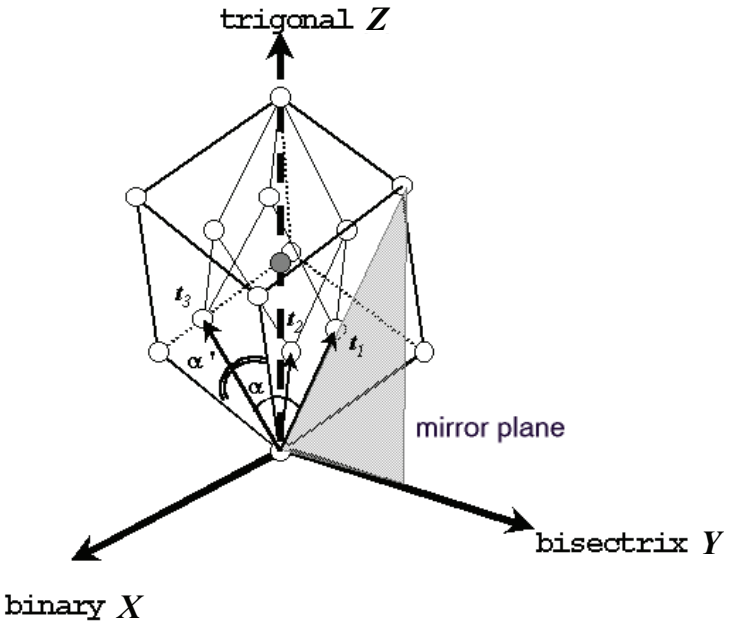

Figure 2-1: The rhombohedral structure of crystals of bismuth, antimony and their alloys $Bi_{1-x}Sb_x$. The trigonal axis (Z-axis), bisectrix axis (Y-axis) and the binary axis (X-axis) form a natural Cartesian coordinate system.

Table 2.1: Crystal parameters for the unit cell of bismuth and antimony.

	rhombohedral cell[39]		hexagonal cell[40]	
	t (Å)	α	a (Å)	c (Å)
antimony	4.5066	$57^\circ 6'$	4.307	11.273
bismuth	4.7459	$57^\circ 14'$	4.547	11.8616

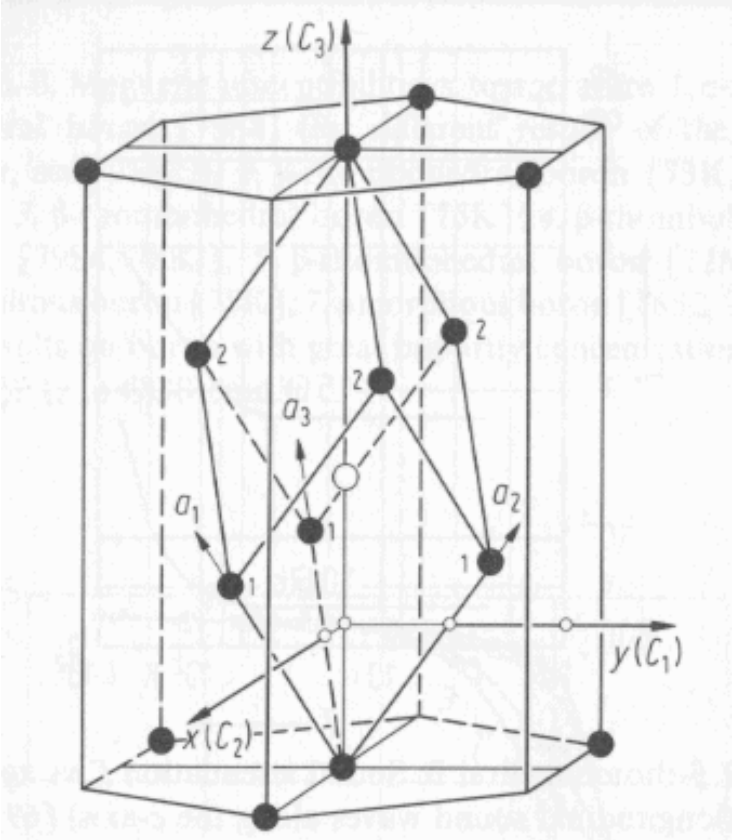

Figure 2-2: The hexagonal coordinates of the rhombohedral structure of the $Bi_{1-x}Sb_x$ crystal.

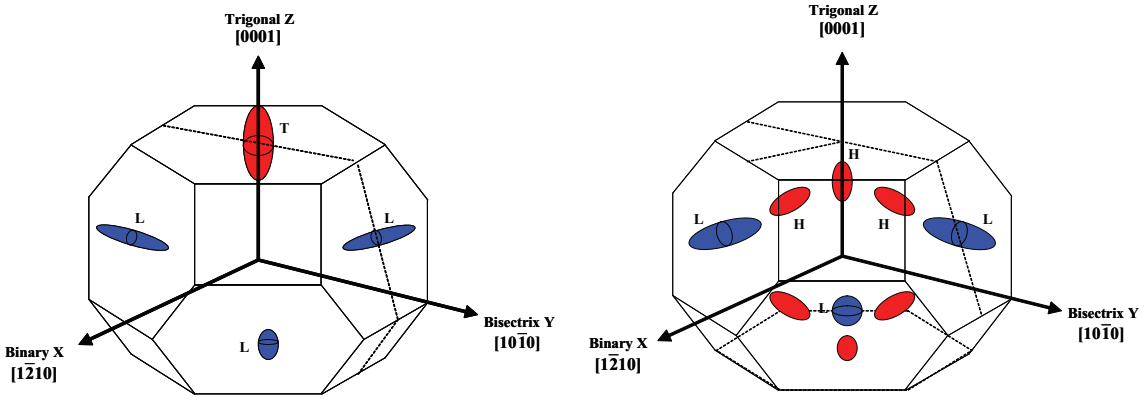

Figure 2-3: The various carrier pocktes in the first Brillouin zone for bulk bismuth and bulk antimony and their alloys

The first Brillouin zone for pure bismuth and the first Brillouin zone for pure antimony are exhibited in Fig. 2-3. The first Brillouin zone for $Bi_{1-x}Sb_x$ can be seen as a Brillouin zone for the FCC lattice compressed along the trigonal axis, because the lattice in real space is elonged along the trigonal axis relative to the related FCC structure [41]. There are one T point, three L points and six H points in the first Brillouin zone [13, 9]. The bottom of the conduction band is located at the L points. The top of the valence band can be located at the T point, the L points or the H points, depending on antimony composition x, temperature T, pressure P and stress [5, 6, 7, 8, 9, 10, 11, 12, 13]. It is meaningfull to start our discussion of the $Bi_{1-x}Sb_x$ system using the cryogenic physical properties of $Bi_{1-x}Sb_x$, because the band structure does not change significantly as a function of temperature when T is below the liquid nitrogen boiling point (77 K) under atmospherical pressure [1]. This assumption significantly simplifies the analysis. In addition, since many experiments have been carrierd out for bulk bismuth, bulk antimony and bulk $Bi_{1-x}Sb_x$ alloys at cryogenic temperatures, the experimental techniques are relatively mature [42, 13, 43, 44, 45, 46, 47]. Thus, I will focus on the cryogenic temperature range under atmospherical pressure in this thesis, if not otherwise mentioned.

Figure 2-4 shows how the band edges at different high symmetry points changes with antimony composition x in 3D bulk $Bi_{1-x}Sb_x$ alloys [1]. When $x < 0.07$, the valence band edge at the T point is above the conduction band edge at the L points, and bulk $Bi_{1-x}Sb_x$ is a semimetal. When $0.07 < x < 0.09$, the valence band edge at the T point is below the

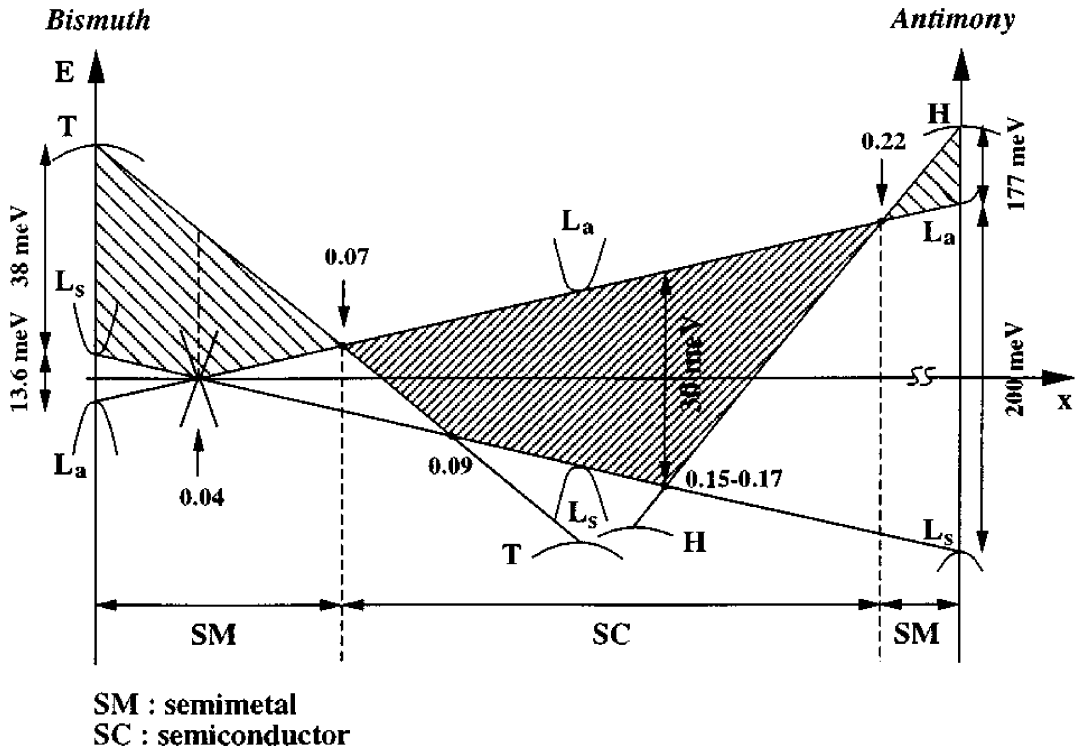

Figure 2-4: How the band edges changes against antimony composition x at the T point, the L points and the H points at cryogenic temperatures below 77 K under atmospherical pressure [1]

conduction band edge at the L points, but above the valence band edge at the L points, so that bulk $Bi_{1-x}Sb_x$ is an indirect-band-gap semiconductor. When $0.09 < x < 0.15$, the valence band edge at the T point and the valence band edge at the H poins are both below the valence band edge at the L points, and bulk $Bi_{1-x}Sb_x$ is a direct-band-gap semiconductor. When $0.15 < x < 0.22$, the valence band edge at the H points is above the valence band edge at the L points, but below the conduction band edge at the L points, so that bulk $Bi_{1-x}Sb_x$ becomes an indirect-band-gap semiconductor again. When $x > 0.22$ the valence band edge at the H points is above the conduction band edge at the L points, so that bulk $Bi_{1-x}Sb_x$ becomes a semimetal. The numerical description of Fig. 2-4 is summarized as

$$E_{T,v}(x) = 45.5 - 551.6 \cdot x \tag{2.1}$$

$$E_{H,v}(x) = -101.36 + 525.8 \cdot x \tag{2.2}$$

$$E_{L,c}(x) = \begin{cases} |484.4 \cdot (x-0.042)^2 - 155.75 \cdot (x-0.042)| & (x \leq 0.17) \\ 4.2136 + 45.8 \cdot x & (x \geq 0.17) \end{cases} \tag{2.3}$$

$$E_{L,v}(x) = -E_{L,c}(x) \quad , \tag{2.4}$$

where the energy unit is meV, the values of the energies are given with respect to the L-point mid-gap energy, and the subscripts c and v stand for the conduction band edges and the valence band edges, respectively [32].

The most interesting phenomenon is that when $x < 0.04$ the L-point band gap decreases with antimony composition x, while when $x > 0.04$ the L-point band gap increases with antimony composition x. At $x = 0.04$ the conduction band edge and the valence band edge exchange their symmetry at the L points, and the L-point band gap E_g^L becomes zero, which leads to the formation of three symmetrical three dimensional Dirac points [7, 14, 1, 15, 16, 17].

2.3 The Effective Mass Tensors Described in a General Coordinate System

In the natural Cartesian coordinate system of bulk $Bi_{1-x}Sb_x$ described in section 2.2, we take the trigonal axis to be the Z axis, the binary axis to be the X axis and the bisectrix axis to be the Y axis. Under the X-Y-Z coordinats system, the effective mass tensor for a certain carrier pocket is generally,

$$\mathbf{M}_{XYZ} = \begin{pmatrix} m_{11} & m_{12} & m_{13} \\ m_{21} & m_{22} & m_{23} \\ m_{31} & m_{32} & m_{33} \end{pmatrix}, \tag{2.5}$$

where $m_{ij} = m_{ji}$. The tensor for the inverse-effective-mass is then

$$\boldsymbol{\alpha}_{XYZ} \equiv \mathbf{M_{XYZ}}^{-1}. \tag{2.6}$$

Now suppose that x-y-z is another coordinate system, the relation between the x-y-z coordinate system and the X-Y-Z coordinate system can be described by Euler Angles β_1, β_2 and β_3, as shown in Fig 2-5. We firstly start from the X-Y-Z coordinate system, and rotate the X-Y-Z axes counter-clockwise by β_1 around the Z axis, then we get X'-Y'-Z. Secondly, we rotate the X'-Y'-Z coordinates around X' counter-clockwise by β_2 to get X'-Y''-z. Thirdly, we rotate X'-Y''-z around Z' couter-clockwise by β_3 to get x-y-z, as indicated in Fig. 2-5.

The effective mass tensor under the x-y-z coordinate system will then be,

$$\mathbf{M}_{xyz} = \mathbf{R_1}\mathbf{R_2}\mathbf{R_3}\mathbf{M}_{XYZ}\mathbf{R_3^*}\mathbf{R_2^*}\mathbf{R_1^*} \tag{2.7}$$

where

$$\mathbf{R_1} = \begin{pmatrix} cos(\beta_1) & sin(\beta_1) & 0 \\ -sin(\beta_1) & cos(\beta_1) & 0 \\ 0 & 0 & 1 \end{pmatrix}, \tag{2.8}$$

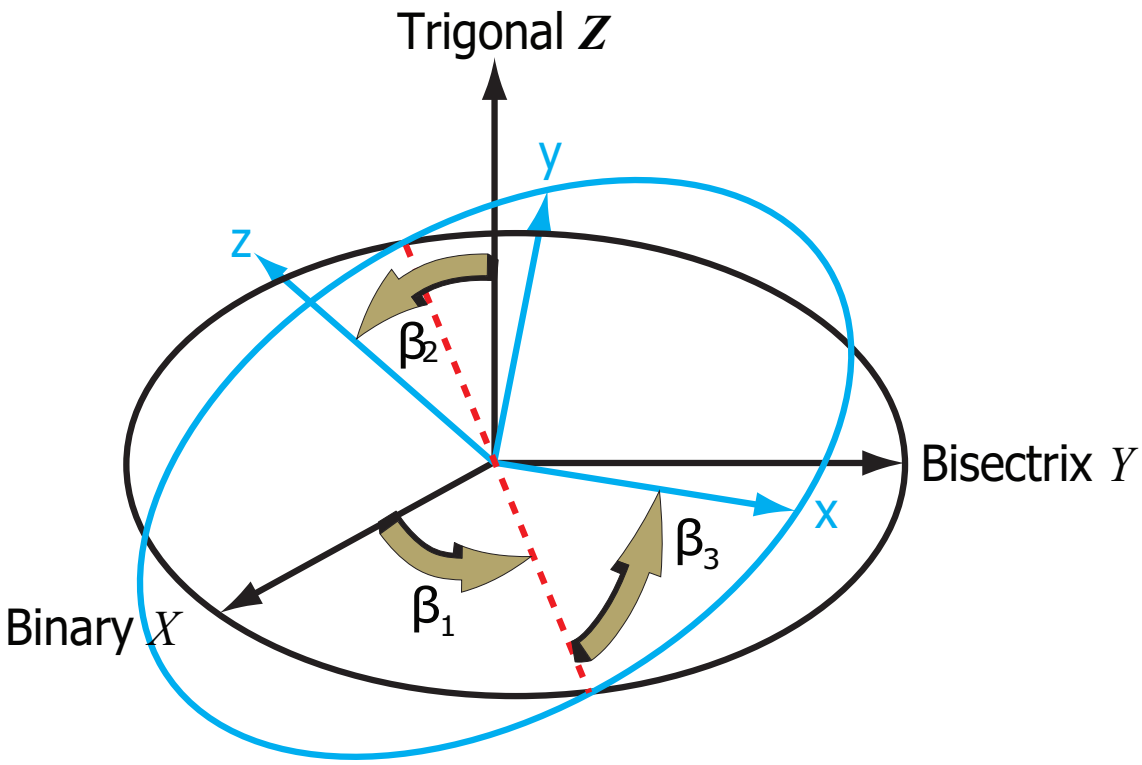

Figure 2-5: The relation between the X-Y-Z coordinate system and the x-y-z coordinate system, described by the Euler angles β_1, β_2 and β_3

$$\mathbf{R_2} = \begin{pmatrix} 1 & 0 & 0 \\ 0 & cos(\beta_2) & sin(\beta_2) \\ 0 & -sin(\beta_2) & cos(\beta_2) \end{pmatrix}, \tag{2.9}$$

and

$$\mathbf{R_3} = \begin{pmatrix} cos(\beta_3) & sin(\beta_3) & 0 \\ -sin(\beta_3) & cos(\beta_3) & 0 \\ 0 & 0 & 1 \end{pmatrix}. \tag{2.10}$$

Similarly,

$$\boldsymbol{\alpha}_{xyz} = \mathbf{R_1}\mathbf{R_2}\mathbf{R_3}\boldsymbol{\alpha}_{XYZ}\mathbf{R_3^*}\mathbf{R_2^*}\mathbf{R_1^*} \tag{2.11}$$

If not otherwise mentioned, we will describe the problem in a general *x*-*y*-*z* coordinate-system, and the the subscript "*xyz*" will be dropped from this point on throughout this entire thesis.

In a film system of $Bi_{1-x}Sb_x$, it is convenient to define a film coordinate system where the *z* axis is along the growth direction, namely normal to the film plane, and the *x*-*y* plane coincides with the film plane, as shown in Fig. 2-6.

2.4 The Lax Model for Bulk Bismuth

For pure bulk bismuth, the bottom of the conduction band is located at the *L* points and the top of the valence band is located at the *T* point. The band structure at the *T* point is parabolically dispersive, which is easy to describe by the effective mass approximation. The band structure at the *L* point is non-parabolically dispersive. In 1960, Cohen and Blount suggested that the properties of the conduction band are mainly determined by its interaction with a single lower level [48]. Using a two-band approximation, the conduction bands become out of phase of with regard tothe de Haas van Alphen formula, which is in agreement with the experiments [49]. Subsequently, Lax and Mavroides estabilished a two-band model for the non-parabolic dispersion relation for the *L*-point carrier pockets [36, 37]. The Lax model shows that the Hamiltonian could be approximately diagonalized,

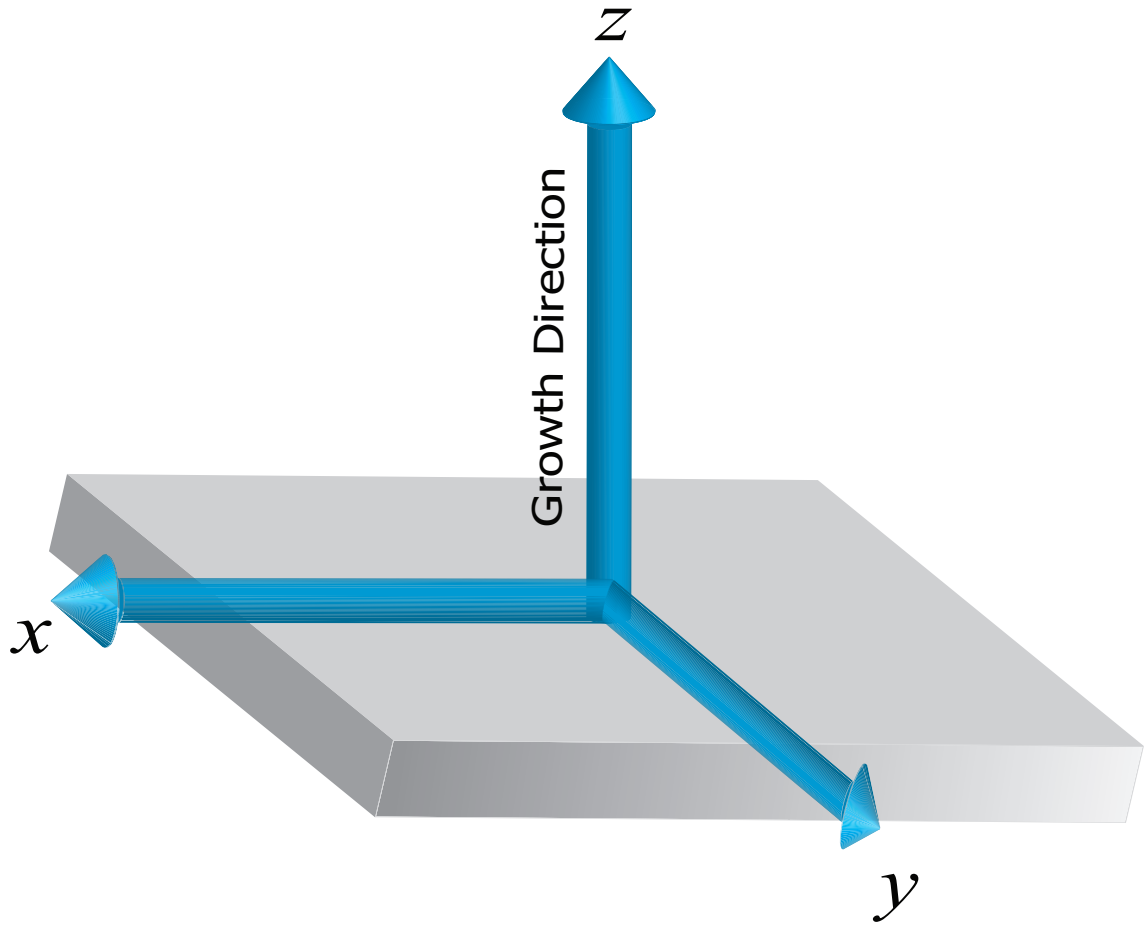

Figure 2-6: The film coordinates where the z axis is normal to the film plane, and the x-y plane coincides with the film plane

which ultimately leads to a very nice and simple form for $E(\mathbf{k})$

$$\mathbf{p}\cdot\boldsymbol{\alpha}\cdot\mathbf{p} = E(\mathbf{k})(1+\frac{E(\mathbf{k})}{E_g}). \tag{2.12}$$

This formula is in agreement with a lot of subsequent experiments [50, 51]. Its simplicity and the high accuracy of this formula makes this model have a high impact on development of this field. The Lax model is based on $\mathbf{k}\cdot\mathbf{p}$ perturbation theory [41]. Because the band gap is narrow, the number of bands that are needed in applying perturbation theory to these dispersion relation is small. Usually a satisfactory representaion over a limited region of $\mathbf{k}$-space has been achieved in terms of the two coupled bands.

Suppose the periodic part of the Bloch function for wave vector $\mathbf{K} = \mathbf{k}_0 + \mathbf{k}$ near $\mathbf{k}_0$ is $u_{n,k}(\mathbf{r})$, where $\mathbf{k}_0$ is the wave vector for a high symmetry point in the first Brillouin zone:

$$[H_0 + H']u_{n,K}(\mathbf{r}) = \varepsilon_n(\mathbf{K})u_{n,K}(\mathbf{r}), \tag{2.13}$$

where the Hamiltonian H_0 at the wave vector $\mathbf{k}_0$ is

$$H_0 = \frac{p^2}{2m} + V(\mathbf{r}) + \hbar\frac{\mathbf{k}_0\cdot\mathbf{p}}{m}, \tag{2.14}$$

the $\mathbf{k}$-dependent operator is

$$H' = \hbar\frac{\mathbf{k}\cdot\mathbf{p}}{m}, \tag{2.15}$$

and the energy eigenvalue $\varepsilon_n(\mathbf{K})$ is related to the eigenvalue of Schrödinger's equation by

$$\varepsilon_n(\mathbf{K}) = E_n(\mathbf{K}) - \hbar^2\frac{\mathbf{k}^2}{2m}. \tag{2.16}$$

In $\mathbf{k}\cdot\mathbf{p}$ pertubation theory, the wave functions $u_{n,K}(\mathbf{r})$ are expanded in terms of band edge wave functions $u_{n,k_0}(\mathbf{r})$, and H' is the perturbation Hamiltonian. Therefore, the strength of the band coupling between the two bands depends on off-diagonal entries of the the momentum matrix. The strongly coupled bands are considered as a nearly degenerate set of levels in the framework of degenerate perturbation theory, and the bands outside the nearly degenerate set are considered as a higher order perturbation. The secular equation

for the two-band model can be assumed to be,

$$\begin{vmatrix} < v|H_0+H'|v > -\varepsilon & < v|H'|c > \\ < c|H'|v > & < c|H_0+H'|c > -\varepsilon \end{vmatrix} = 0 \quad , \tag{2.17}$$

where

$$< i|H_0+H'|i >= \pm\frac{\varepsilon_g}{2} + \frac{\hbar^2\mathbf{k}^2}{2m} + \frac{\hbar\mathbf{k}}{m}\cdot < i|\mathbf{p}|i > \tag{2.18}$$

and i is the band index that can be c or v, which stand for the conduction band and the valence band, respectively. Solution of this secular equation yields the dispersion relation for the coupled two bands,

$$\varepsilon_i(\mathbf{k}) = \frac{E_c+E_v}{2} \pm \frac{1}{2}[(E_c+E_v)^2 + \frac{\hbar^2}{m^2}\mathbf{k}\cdot\mathbf{P}^2\cdot\mathbf{k}]^{\frac{1}{2}}, \tag{2.19}$$

where the tensor $\mathbf{P}^2$ is defined by the off-diagonal entries of the momentum matrix that connects the strongly coupled bands,

$$\mathbf{P}^2 =< c|\mathbf{p}|v >< v|\mathbf{p}|c > . \tag{2.20}$$

2.5 The development of the Iterative-Two-Dimensional-Two-Band Model

For $Bi_{1-x}Sb_x$ thin films, the two-dimensional electronic band structure varies also as a function of film thickness and film growth orientation, which provides considerable flexibility compared to bulk $Bi_{1-x}Sb_x$. Furthermore, the quantum confinement effect in the thin film system is potentially interesting, where its anisotropic properties imply potential application possibilities.

The energy spectrum near an L-point Dirac cone in a $Bi_{1-x}Sb_x$ thin film is calculated

Table 2.2: The effective mass tensor components for bulk $Bi_{1-x}Sb_x$ alloys at $T \leq 77$ K.

Parameters	Notation	Value	Reference
L-point carrier effective mass tensor components at the band edge (bulk bismuth, x=0)[a]	m_{xx}	$0.00119\,m_0$	[52]
	m_{yy}	$0.263\,m_0$	
	m_{zz}	$0.00516\,m_0$	
	m_{yz}	$0.0274\,m_0$	
T-point hole effective mass tensor components at the band edge	m_{xx}	$0.059\,m_0$	[45]
	m_{yy}	$0.059\,m_0$	
	m_{zz}	$0.634\,m_0$	
H-point hole effective mass tensor components at the band edge	m_{xx}	$0.068\,m_0$	[46]
	m_{yy}	$0.63\,m_0$	
	m_{zz}	$0.34\,m_0$	
	m_{yz}	$0.41\,m_0$	

[a] For other values of x, the mass tensor is modified to account for the dependence of the non-parabolicity of the band structure at the L-point on the bandgap energy, E_g^L.

based on the iterative-two-dimensional-two-band model described below. Here the general two band model for two strongly coupled bands obeys the relation in Eq. 2.12. We will from this point onward set $\hbar$ to be 1 for convenience. The two coupled key parameters $\boldsymbol{\alpha}$ and E_g are calculated in an iterative way in our model as

$$\boldsymbol{\alpha}^{[n]} = \frac{E_g^{[n-1]}}{E_g^{[n]}} \cdot \boldsymbol{\alpha}^{[n-1]} + \frac{1}{m_0} \cdot (1 - \frac{E_g^{[n-1]}}{E_g^{[n]}}) \cdot \mathbf{I} \tag{2.21}$$

and

$$E_g^{[n+1]} = E_g^{[n]} + 2 \cdot \frac{\pi^2 \alpha_{33}^{[n]}}{2 \cdot l_z^2}, \tag{2.22}$$

where m_0 is the free electron mass, $\mathbf{I}$ is the identity matrix, l_z is the film thickness and n denotes the nth step in the iteration. The procedure is repeated until $\boldsymbol{\alpha}^{[n]}$ and $E_g^{[n]}$ become self-consistent, and then we get accurate solutions for $\boldsymbol{\alpha}^{film}(Bi_{1-x}Sb_x) = \boldsymbol{\alpha}^{[n]}$ and $E_g^{film}(Bi_{1-x}Sb_x) = E_g^{[n]}$ for thin film $Bi_{1-x}Sb_x$. Because of the approximations

$$\frac{1}{m_0} \cdot (1 - \frac{E_g^{[n-1]}}{E_g^{[n]}}) \cdot \mathbf{I} \ll \frac{E_g^{[n-1]}}{E_g^{[n]}} \cdot \boldsymbol{\alpha}^{[n-1]}$$

and

$$\left| E_g^{[n+1]} - E_g^{[n]} \right| \ll 2 \cdot \frac{\pi^2 \alpha_{33}^{[n]}}{2 \cdot l_z^2}$$

that are valid for antimony composition $0 \leq x \leq 0.10$, Eqs. (2.21) and (2.22) can be further simplified, which converge to the analytical solution as

$$\boldsymbol{\alpha}^{film}(Bi_{1-x}Sb_x) = \frac{\boldsymbol{\alpha}^{bulk}(Bi)}{E_g^{film}(Bi_{1-x}Sb_x)} \cdot E_g^{bulk}(Bi) \tag{2.23}$$

and

$$E_g^{film}(Bi_{1-x}Sb_x) = E_g^{bulk}(Bi_{1-x}Sb_x) + \frac{\pi^2 \alpha_{33}^{film}(Bi_{1-x}Sb_x)}{l_z^2}. \tag{2.24}$$

The dispersion relation $E(\mathbf{k})$ can then be then solved by the methods used by Ref. [34, 30] from

$$E(\mathbf{k}) + \frac{E^2(\mathbf{k})}{E_g^{film}} = \frac{1}{2}\mathbf{k}^* \cdot \tilde{\boldsymbol{\alpha}} \cdot \mathbf{k} + \frac{\pi^2 \alpha_{33}}{2 l_z^2}, \tag{2.25}$$

where $\tilde{\alpha}_{ij} = \alpha_{i3}\alpha_{j3}/\alpha_{33} - \alpha_{ij}$ for $i, j = 1$ and 2, and $\boldsymbol{\alpha} = \boldsymbol{\alpha}^{film}(Bi_{1-x}Sb_x)$. The Hamiltonian for Bi and $Bi_{1-x}Sb_x$ based on $\mathbf{k} \cdot \mathbf{p}$ theory in Eq. 2.12 is equivalent to a Dirac Hamiltonian with a scaled canonical conjugate momentum [53]. Thus, Eq. (3.1) is also a good approximation to describe the Dirac cones. The band parameters we use in the present calculations are values that were measured by cyclotron resonance experiments, which are listed in Table 2.2.

2.6 The Extension of the Iterative-Two-Dimensional-Two-Band Model to a General Non-Parabolic Low-Dimensional System

There are many other narrow-band materials systems that have strongly coupled bands at the band edges where the dispersion relations are non-parabolic or even linear, for example the X-point dispersion relation of $Si_{1-x}Ge_x$ [54] and the L-point dispersion relation of PbTe [55].

When these narrow-band materials are synthesized in 2D thin films, the problem to describe the 2D non-parabolic dispersion relations are in many ways similar as the problem in $Bi_{1-x}Sb_x$ thin films, as I describe here in this thesis. Thus, the iterative-two-dimensional-two-band model can be extended to other narrow-band thin films.

For other low-dimensional systems, as for example, one-dimensional nano-wires, the iterative procedure between α and E_g is similar too. An iterative-one-dimensional-two-band model can then be similarlly developed [56].

Chapter 3

Constructing Anisotropic Single-Dirac-Cones in $Bi_{1-x}Sb_x$ Thin Films

3.1 Introduction

Materials with two-dimensional Dirac cones in their electronic band structures have recently attracted considerable attention. Many important novel physical studies have been carried out on both massless and massive 2D Dirac fermions, including studies of the half-integer quantum Hall effect [57, 58], the anomalous absence of back scattering, the Klein paradox effect [59], high temperature superconductivity [60], and unusual microwave response effects [20]. The ultrahigh carrier mobility of Dirac fermions in graphene offers new opportunities for a variety of electronics applications [42]. Recently, 2D Dirac cones observed in topological insulators have identified this class of materials as candidates for quantum computation, spintronics, novel superconductors and thermoelectrics [61, 62, 63, 64, 65].

Materials with 2D single-Dirac-cones, especially 2D anisotropic single-Dirac-cones, are of special interest. Simulations with ultracold atoms trapped on optical lattices have been used to study general 2D single-Dirac-cones [66]. It is believed that graphene su-

perlattice materials, which are described by anisotropic 2D single-Dirac-cones, could potentially be developed for use in nano-electronic-circuits without requiring the cutting processes, and in desktop experiments that simulate high-energy relativistic particles propagating in an anisotropic space [67].

Among all materials candidates that may possibly make anisotropic single-Dirac-cones, 2D $Bi_{1-x}Sb_x$ thin films are especially attractive. Firstly, it has been proved that the band structure of three-dimensional bulk $Bi_{1-x}Sb_x$ can be varied as a function of antimony composition x, temperature, pressure and strain, and the Fermi level can be adjusted to change the electronic properties [13, 5, 6, 10, 43, 12]. Secondly, not only have bulk state Dirac points been studied in bulk $Bi_{1-x}Sb_x$ alloys [16, 44, 68], but also the first observation of a surface state 2D single-Dirac-cone for a topological insulator was made in bulk $Bi_{0.9}Sb_{0.1}$ [18]. Some 2D experiments on $Bi_{1-x}Sb_x$ thin films grown normal to the trigonal direction have already been carried out [69, 70, 71]. However, possible Dirac-cone materials of 2D $Bi_{1-x}Sb_x$ thin films have not yet been studied. It is meaningful to start from the cryogenic physical properties of 2D $Bi_{1-x}Sb_x$, because the band structure does not change significantly with temperature when T is below the liquid nitrogen boiling point (77 K), which significantly simplifies the analysis. In addition, since many experiments have been carried out for bulk Bi and $Bi_{1-x}Sb_x$ at cryogenic temperatures, the experimental techniques are relatively mature. Thus, it would be easy to experimentaly realize the theoretical predictions in 2D $Bi_{1-x}Sb_x$ in this temperature range.

In this chapter, we focus on the cryogenic temperature range. We have systematically studied how the properties of the 2D L-point single-Dirac-cones in $Bi_{1-x}Sb_x$ thin films, such as their anisotropies and linear $E(\mathbf{k})$, change with the film thickness and the growth orientation. We have also discovered that single-Dirac-cones with different anisotropies can be constructed in $Bi_{1-x}Sb_x$ thin films.

3.2 Anisotropic Single-Dirac-Cones in $Bi_{1-x}Sb_x$ Thin Films

There are three symmetrical L points in the first 3D Brillouin zone of $Bi_{1-x}Sb_x$ as shown in Fig. 3-1. In order to get a single-Dirac-cone, we need to grow the $Bi_{1-x}Sb_x$ thin film normal

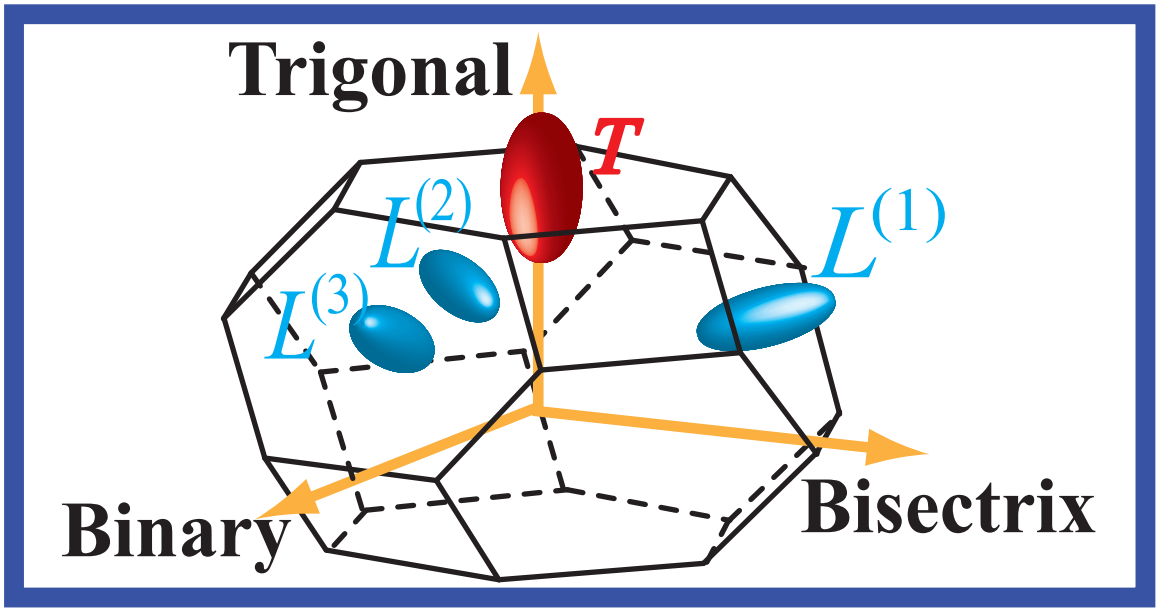

Figure 3-1: The 3-fold degenerate L points and the T point in the first Brillouin zone of bulk $Bi_{1-x}Sb_x$.

to a low symmetry crystalline direction so that we can have a single L-point that differs from the other two by breaking the 3-fold symmetry occurring in 3D. Moreover, the two quantities in Eq. 2.22 need to be minimized, namely the bulk-band-gap term $E_g^{bulk}(Bi_{1-x}Sb_x)$ and the quantum-confinement-induced term $h^2\alpha_{33}^{[0]}/4 \cdot l_z^2$ for this special single L-point. Thus, growing a film normal to the bisectrix direction is a good way to do this, where the 3-fold symmetry is broken and the α_{33} inverse mass component is near its minimum; this calculation is discussed below. Minimizing the value of bulk term $E_g^{bulk}(Bi_{1-x}Sb_x)$ by varying temperature T, pressure P and antimony composition x has been discussed in the literature [5, 6, 7, 8, 9, 10, 11, 12, 13], especially for the case of x=0.04, where $E_g^{bulk}(Bi_{1-x}Sb_x)$ decreases to 0 at cryogenic temperatures under atmospheric pressure. Thin films with the composition $Bi_{0.96}Sb_{0.04}$ have already been synthesized in experiments by researchers in the Ukraine [71], for films grown normal to the trigonal direction. The model that we have developed in Chapter 2 is valid for all values of antimony composition x (≤ 0.15). However, for the convenience of experimentalists to use our theoretical predictions, in this chapter, we illustrate simple examples of single-Dirac-cones that can be found in $Bi_{0.96}Sb_{0.04}$. More generally, $Bi_{1-x}Sb_x$ thin films of other antimony compositions x can be modeled in the similar way.

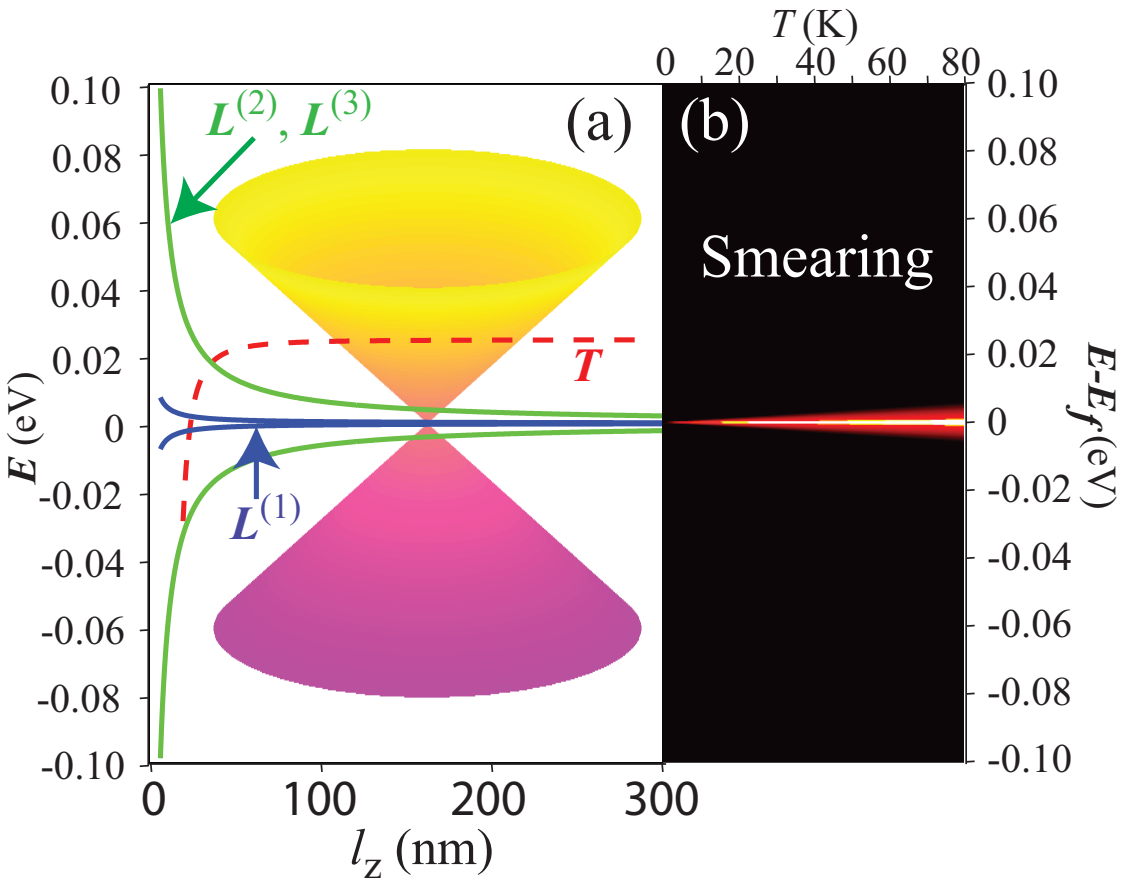

Figure 3-2: How the $L^{(1)}$-point single-Dirac-cone is formed. (a) shows the band structure of a $Bi_{0.96}Sb_{0.04}$ thin film grown normal to the bisectrix axis and how the band structure changes over different film thickness. The green curves show the lowest conduction band (upper one) and the highest valence band (lower one) at the $L^{(2)}$ and $L^{(3)}$ points. The blue curves are for the $L^{(1)}$ point valence band and conduction band as a function of film thickness. The dashed red curve is the highest valence band at the T point. The $L^{(1)}$-point band gap remains less than the order of ~ 1 meV until the film thickness l_z is very small. The $L^{(2)}$ and $L^{(3)}$ points have the same band gap, which is largely opened up. Thus, an anisotropic single-Dirac-cone is formed at the $L^{(1)}$ point when the film thickness l_z is large enough to retain the $L^{(1)}$-point mini-gap essentially zero, i.e. less than ~ 1 meV.(b) shows the thermal smearing $(-\frac{\partial f_0}{\partial E})$ of the Fermi-Dirac distribution as a function of cryogenic temperature (top scale). For comparison between (a) and (b), the Fermi level E_f is aligned with $E = 0$, i.e. the middle point of the L-point band gap. Cases where the Fermi level E_f is at other positions can be discussed in the similar way. Only carriers within smearing will get excited and contribute to the transport phenomena.

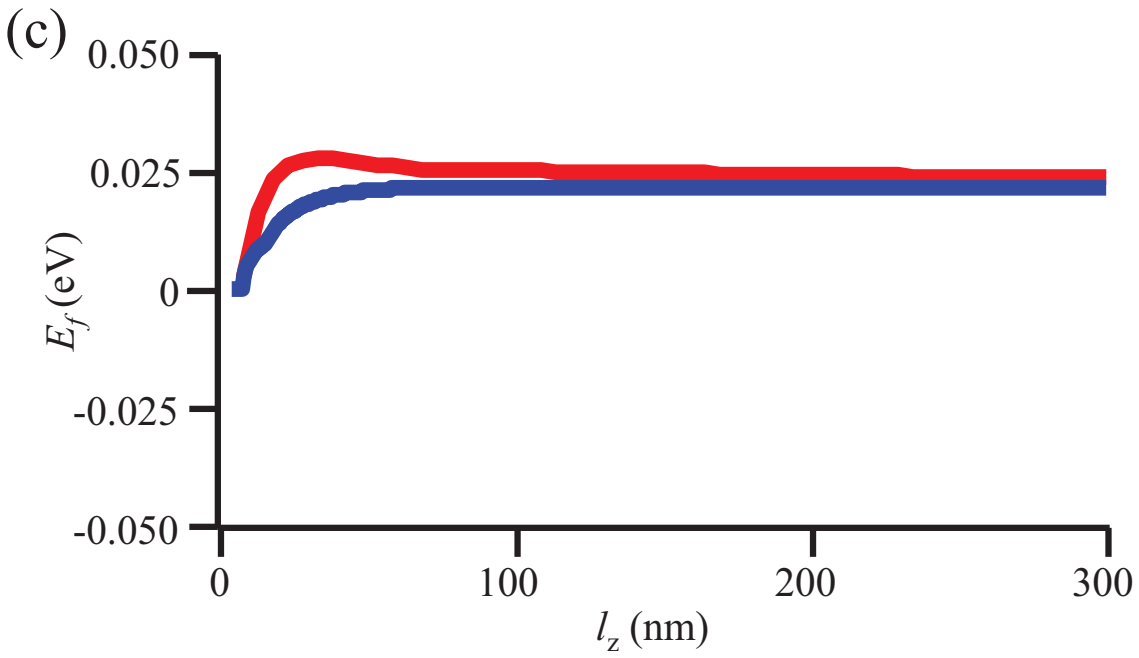

Figure 3-3: If no doping is added and no gate voltage is applied, the l_z dependence of the intrinsic Fermi levels is shown at 77 K (red curve) and at 4.2 K (blue curve).

Based on our model, a single 2D Dirac cone can be constructed in a $Bi_{0.96}Sb_{0.04}$ thin film normal to the bisectrix axis. For this thin film the 3-fold symmetry of the L points in reciprocal space is broken. According to our calculations, the $L^{(1)}$-point band gap $E_g^{L^{(1)}}$ will not exceed $\sim$ 1 meV until the film is thinner than 80 nm. However, our calculations in this thesis show that the $L^{(2)}$- and $L^{(3)}$-point band gaps $E_g^{L^{(2)}}$ ($E_g^{L^{(2)}} = E_g^{L^{(3)}}$) will open up and increase significantly when the film thickness decreases. When $l_z = 300$ nm, $E_g^{L^{(2)}}$ is already larger than 7 meV, while $E_g^{L^{(1)}}$ is still smaller than 0.1 meV. This means that a single-Dirac-cone is formed at the $L^{(1)}$ point as shown in Fig. 3-2(a).

Up to now, we have only discussed the band structure and the dispersion relations at the L points. Another important aspect is the Fermi level E_f, which determines the carrier density and the transport properties. The Fermi level for a $Bi_{1-x}Sb_x$ thin film changes with film thickness, temperature, external gate voltage and impurity doping. For further discussion of how the Fermi level influences the physical properties of the single-Dirac-cone, we assume that the Fermi level for a specific $Bi_{1-x}Sb_x$ thin film can be varied freely within the range of 0 to 25 meV without destroying the single-Dirac-cone. How the carrier

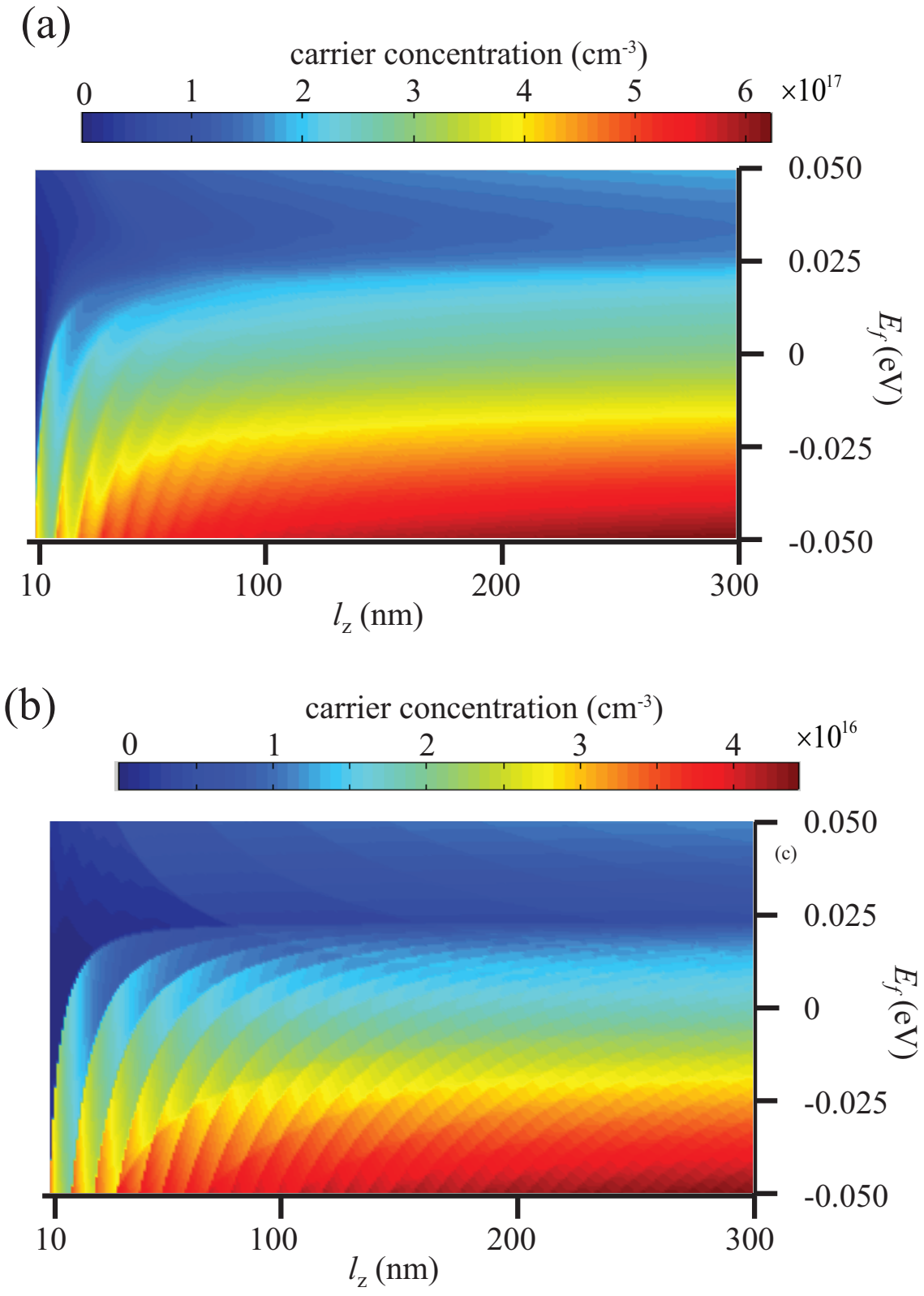

Figure 3-4: Carrier concentration of $Bi_{0.96}Sb_{0.04}$ vs. film thickness l_z and Fermi level E_f are shown at (a) 77 K and (b) 4.2 K. The curves are drawn for films differing in thickness from one another by 10 nm and the carrier concentration is given in terms of the indicated color code.

concentration changes with film thickness and temperature will be discussed later.

The carriers that contribute to transport are the ones that are within the smearing of the Fermi-Dirac distribution function $(-\frac{\partial f_0}{\partial E})$, where $f_0 = (1 + exp[(E - E_f)/k_B \cdot T])^{-1}$. The quantity $(-\frac{\partial f_0}{\partial E})$ is very sharp over E at cryogenic temperatures as shown in Fig. 3-2(b), and has a width in the order of $\sim k_B \cdot T$. For comparison to Fig. 3-2(a), we have aligned the Fermi level in Fig. 3-2(b) with $E = 0$ to indicate the absence of carrers due to dopants. In this case, the Fermi level is at the apex of the $L^{(1)}$-point single-Dirac-cone. Then the Dirac fermions which contribute to transport will only come from this $L^{(1)}$-point single-Dirac-cone, and not from the $L^{(2)}$ or $L^{(3)}$ points, at cryogenic temperatures.

Figure 3-3 shows the Fermi level for intrinsic $Bi_{0.96}Sb_{0.04}$ films without doping or gate votage. At cryogenic temperatures, the intrinsic Fermi level starts to drop with film thickness when the film is thinner than $\sim$40 nm, which reveals the semimetal-semiconductor transition, where the T-point valence band falls below the $L^{(1)}$-point conduction band, consistent with the prediction of Fig. 3-2(a).

How the carrier concentration for a $Bi_{0.96}Sb_{0.04}$ film changes as a function of film thickness and Fermi level is calculated next. Figure 3-4 (a) and (b), respectively, show the total carrier concentrations for a $Bi_{0.96}Sb_{0.04}$ film at the liquid nitrogen boiling point (77 K) and the liquid helium boiling point (4.2 K). The overall carrier concentration is very low ($\sim 10^{17}$ cm^{-3}) at 77 K in Fig. 3-4(a) and much lower ($\sim 10^{16}$ cm^{-3}) at 4.2 K in Fig. 3-4(b).

There are two kinds of Dirac fermions associated with a Dirac cone that researchers are interested in, the massless Dirac fermions and the massive Dirac fermions. The massless Dirac fermions are the fermions that are right at the apex of a Dirac cone. Other Dirac fermions that are at the Dirac cone but not at the apex are massive. In experiments, a Dirac cone is usually not perfect. A mini-gap often exists which induces a mini-mass at the apex of the Dirac cone. Such an effect also occurs in single layer graphene [57, 58]. Therefore, practically, there are two main features that characterize the quality of a Dirac cone, the mini-mass for the "massless" Dirac fermions occuring at the apex, and the fermion velocity $\mathbf{v}(\mathbf{k})$ as a function of $\mathbf{k}$ for the massive Dirac fermions. Because the fermions are linearly dispersed near a Dirac cone, $\mathbf{v}(\mathbf{k})$ should only be a function of the direction of $\mathbf{k}$ in $Bi_{1-x}Sb_x$ thin films. The anisotropy of the Dirac cone can be characterized by the ratio between the

maximum and minimum $\mathbf{v}(\mathbf{k})$.

The $L^{(1)}$-point anisotropic single-Dirac-cone in a 300 nm thick $Bi_{1-x}Sb_x$ thin film grown normal to the bisectrix axis has a linear $E(\mathbf{k})$ behavior with a very sharp apex [Fig. 3-5(a)]. In this film, k_x and k_y represent the trigonal axis and the binary axis, respectively. $E_g^{L^{(1)}}$ for this Dirac cone is smaller than 0.1 meV, and the effective mass at the apex of the Dirac cone is $\sim 10^{-5} m_0$, which can be considered as essentially gapless and massless. We have also calculated the $\mathbf{v}(\mathbf{k})$ relation of the Dirac fermions for different values of momentum [Fig. 3-5(b)]. For the anisotropy of this single-Dirac-cone, it can be seen that the maximum and minimum of $\mathbf{v}(\mathbf{k})$ are $1.6 \cdot c_{light}/300$ (along k_x) and $1.1 \cdot c_{light}/300$, (along k_y), respectively, which differs by a factor of $\sim$1.5, where c_{light} is the speed of light.

The contribution of the $L^{(1)}$-point single-Dirac-cone fermions to the transport properties is much greater than that contributed by the parabolically dispersed fermions at the T point. In bulk Bi and $Bi_{1-x}Sb_x$ at cryogenic temperatures, it has been shown both theoretically and experimentally that the transport properties are dominated by the L-point carriers, which have ultra-high electron and hole mobilities [47, 72, 73], because of the ultra-large carrier group velocities of the $L^{(1)}$ point carriers ($\sim 10^{-2} \cdot c_{light}$). This is not difficult to understand and can be explained in a very simple manner. For example, the electronic conductivity of the carriers for a specific carrier pocket is

$$\sigma_{ij} = e^2 D_{E_f} \cdot v_i \cdot \sum_l (\tau_{E_f})_{jl} \cdot v_l, \tag{3.1}$$

where τ_{E_f} and D_{E_f} are, respectively, the anisotropic relaxation time tensor and the density of states for carriers of this specific carrier pocket at the Fermi level E_f, and i , j and l denote components of the various vector and tensor quantities. We take the principal axis along k_x as an example, i.e. $i = j = x$ and $\sigma_{xx} = e^2 D_{E_f} (\tau_{E_f})_{xx} \cdot v_x^2$. In Bi and $Bi_{1-x}Sb_x$, the relaxation time $(\tau_{E_f})_{xx} = \lambda_{xx} v_x^{-1}$, where λ_{xx} is the mean free path and $\lambda_{xx} \propto D_{E_f}^{-1}$. Thus, we have $\sigma_{xx} \propto v_{x(E_f)}$, where $v_{x(E_f)}$ is the carrier group k_x direction velocity component for this specific carrier pocket at the Fermi level E_f. For the $L^{(1)}$-point single-Dirac-cone, $v_{x(E_f)}^{[Dirac]} \sim 10^{-2} \cdot c_{light}$, while for the T-point parabolic pocket, $v_{x(E_f)}^{[T]} \sim 10^3$ m/s, thereby explaining why $\sigma_{xx}^{[Dirac]} \gg \sigma_{xx}^{[T]}$.

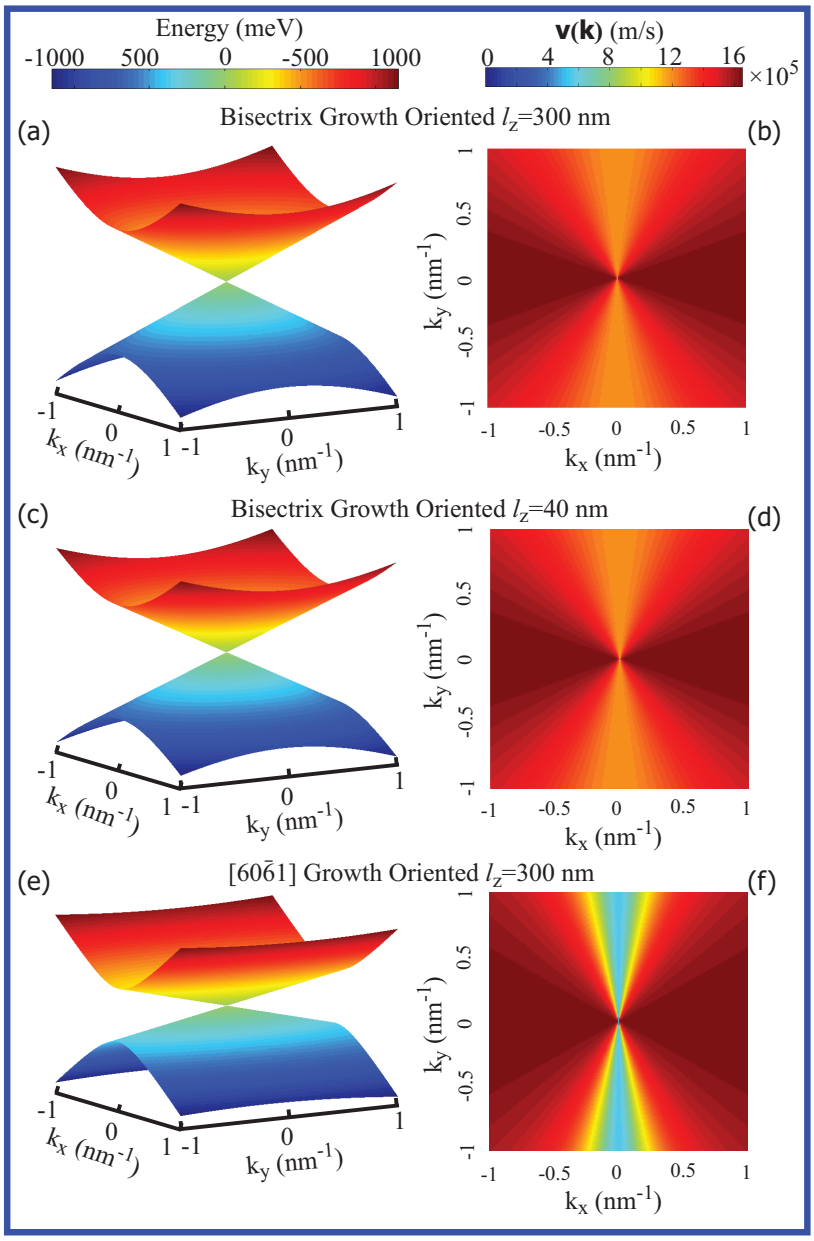

Figure 3-5: Different anisotropic single-Dirac-cones in different $Bi_{0.96}Sb_{0.04}$ thin films: (a) and (b) describe a sharp-apex $L^{(1)}$-point anisotropic single-Dirac-cone in a 300 nm thick $Bi_{0.96}Sb_{0.04}$ film grown normal to the bisectrix axis. For convenience, the origin of momentum $\mathbf{k}$ is chosen to be at the $L^{(1)}$ point. (c) and (d) describe an $L^{(1)}$-point anisotropic single-Dirac-cone where the T-point carrier-pocket is totally below the $L^{(1)}$-point Dirac cone, in a 40 nm thick $Bi_{0.96}Sb_{0.04}$ film grown normal to the bisectrix axis. (e) and (f) describe a highly anisotropic single-Dirac-cone in a 300 nm thick $Bi_{0.96}Sb_{0.04}$ film grown normal to the $[60\bar{6}1]$ crystalline direction. (a), (c) and (e) show the dispersion relations of these single-Dirac-cones. (b), (d) and (f) show the group velocities $\mathbf{v}$ of Dirac fermions over different momenta $\mathbf{k}$. (c)-(d) are not significantly different from (a)-(b), but (e)-(f) are obviously more anisotropic than (a)-(b) and (c)-(d).

Moreover, the T-point parabolically dispersed carrier pocket can also be moved further down in energy below the $L^{(1)}$-point single-Dirac-cone, in a 2D $Bi_{0.96}Sb_{0.04}$ thin film, which is not achieved in bulk $Bi_{0.96}Sb_{0.04}$. When the film thickness decreases, the top point of the T-point valence band decreases in energy much faster than the $L^{(1)}$-point valence band as shown in Fig. 3-2(a). When the film thickness is less than 40 nm, the T-point valence band is totally below the bottom of the $L^{(1)}$-point conduction band, indicating a semimetal-semiconductor transition The effective mass at the apex of this single-Dirac-cone is $\sim 10^{-4}m_0$, which is still essentially massless. The corresponding Dirac cone is plotted in Fig. 3-5(c), as well as the velocity vs. momentum relation $\mathbf{v}(\mathbf{k})$ for the massive Dirac fermions as in Fig. 3-5(d). The linearity and the anisotropy of the Dirac cone is not notably influenced by film thickness for a film of $l_z = 40$ nm, as can be seen by comparing Figs. 3-5(c) and (d) to Figs. 3-5(a) and (b), respectively, showing that very thin films are needed to show quantum confinement (below 40 nm).

In some applications, e.g. in nano-electronic-circuit design, a higher anisotropy of the Dirac cone could be required. For a $Bi_{0.96}Sb_{0.04}$ thin film, the $L^{(1)}$-point $E(\mathbf{k})$ has a smaller mini-mass at the apex but a lower anisotropy if the film is grown normal to the bisectrix axis, while the $L^{(1)}$-point $E(\mathbf{k})$ has a larger mini-mass at the apex but a higher anisotropy if the film is grown normal to the trigonal axis. This gives us an idea that a film grown normal to a crystalline direction between the trigonal axis and the bisectrix axis, would have both a small mini-mass and a high anisotropy. As an example, we illustrate in Fig. 3-5(e) and (f) a film grown normal to a low-symmetrical crystalline direction $\hat{\mathbf{n}}$, where $\hat{\mathbf{n}}$ is in the binary plane, making an angle of 14° to the bisectrix axis and 76° to the trigonal axis. In the hexagonal notation system for the rhombohedral $Bi_{1-x}Sb_x$, the trigonal axis is $[0001]$ and the bisectrix axis is $[10\bar{1}0]$. Thus, $\hat{\mathbf{n}}$ can be denoted as $[60\bar{6}1]$. Here $\hat{\mathbf{n}}$ is just a randomly chosen crystalline direction within the trigonal-bisectrix plane to be an example, other crystalline directions can be discussed in the similar way. Figure 3-5(e) and (f) illustrate a 300 nm thick film grown normal to $\hat{\mathbf{n}}$, where k_y is still along the binary axis, while k_x is in the direction perpendicular to both the binary axis and $\hat{\mathbf{n}}$. Then $E_g^{L^{(1)}}$ for this Dirac cone [Fig. 3-5(e)] is smaller than 0.46 meV, and the mini-mass at the apex of the Dirac cone is still negligible ($\sim 10^{-4}m_0$). The anisotropy for this single-Dirac-cone

[Fig. 3-5(e)] is much higher. The maximum and minimum values of $\mathbf{v}(\mathbf{k})$ for the massive Dirac fermions are $1.65 \cdot c_{light}/300$ and $0.55 \cdot c_{light}/300$, respectively, which differ by a factor of $\sim$3 [Fig. 3-5(f)].

The technology for experimental implementations of the $Bi_{1-x}Sb_x$ thin films we described above is foreseeable. Single crystal bismuth and $Bi_{1-x}Sb_x$ thin films grown normal to the trigonal axis have been synthesized [71], and so have single crystal Bi and $Bi_{1-x}Sb_x$ nanowires grown along various crystalline directions [33, 74, 75, 76, 77, 78, 79, 80, 81, 35]. The cryogenic measurement of transport, optical and magnetic properties of bulk bismuth and $Bi_{1-x}Sb_x$ have also been developed to a very high level of sophistication over decades of effort [13, 42, 43, 44, 45, 46, 47].

3.3 Conclusion

In conclusion, based on the iterative-two-dimensional-two-band we have developed in Chapter 2, we have made a prediction that anisotropic single-Dirac-cones can be constructed in $Bi_{1-x}Sb_x$ thin films. Some critical cases of $L^{(1)}$-point single-Dirac-cones are illustrated as examples. Novel physical phenomena associated with massless and massive Dirac fermions that have been previously reported in other materials systems could hopefully also be observed in $Bi_{1-x}Sb_x$ thin films. Because the $Bi_{1-x}Sb_x$ thin film system has special features as we discussed above, we can also expect to observe new physical phenomena that have never been observed in other systems.

Chapter 4

Constructing a Large Variety of Dirac-Cone Materials in the $Bi_{1-x}Sb_x$ Thin Film System

4.1 Introduction

In an electronic band structure, if the dispersion relation $E(\mathbf{k})$ can be described by a linear function as $E = \mathbf{v} \cdot \mathbf{k}$, where $\mathbf{v}$ is the velocity matrix and $\mathbf{k}$ is the lattice momentum, the point where $E \to 0$ is called a Dirac point. In a two-dimensional system, a 2D projection of a Dirac point is called a Dirac cone. A single-, bi- or tri-Dirac cone system has one, two or three different Dirac cones that are degenerate in energy in its first Brillouin zone. For example, a single sheet graphene has two degenerate isotropic Dirac cones at Points K and K' in its first Brillouin zone, so it is considered as a bi-Dirac-cone system. Dirac fermions can be immune to localization effects and can propagate without scattering over large distances on the order of micrometers [82], which is essentially important to electronic applications. Dirac-cone materials are considered as promising materials for the next generation of electronic industry. In this chapter, we show how to construct a large variety of Dirac-cone materials, including bi-Dirac-cone materials, tri-Dirac-cone materials, quasi-Dirac-cone materials and semi-Dirac-cone materials, based on the $Bi_{1-x}Sb_x$ thin

film system, we will still use the $Bi_{0.96}Sb_{0.04}$ thin films at cryogenic temperatures under atmospherical pressure in giving examples of the different types of Dirac cones that can be made.

4.2 Constructing a Large Variety of Dirac-Cone Materials

According to Eqs. 2.12 and 3.1, when $E_g \to 0$ at an L point, the electronic dispersion relation becomes a perfect Dirac cone, where the energy E is exactly proportional to the lattice momentum $\mathbf{k}$ measured from that L point. When E_g becomes large enough, the linearity of the dispersion relation becomes an approximation, and the Dirac cone becomes a quasi-Dirac cone. If $\tilde{\alpha}_{11} \gg \tilde{\alpha}_{22}$ with a finite E_g, so that $E \propto k_x$ and $E \propto k_y^2$, we call it a semi-Dirac cone. In a semi-Dirac cone, the fermions are relativistically dispersive in one direction (k_x), and classically dispersive in another direction (k_y).

We propose that single-, bi- and tri-Dirac-cone materials can be constructed from $Bi_{1-x}Sb_x$ thin films, by proper synthesis conditions to control the relative symmetries of the three L points. $Bi_{1-x}Sb_x$ thin films grown along the bisectrix axis can be single-Dirac-cone materials, as illustrated in Fig. 4-1(a), where the 3-fold degeneracy of the $L^{(1)}$, $L^{(2)}$ and $L^{(3)}$ points is broken. The value of the film-direction-inverse-mass-component $\alpha_{33}^{film}(Bi_{1-x}Sb_x)$ is much smaller for the $L^{(1)}$ point than the corresponding values for the $L^{(2)}$ and $L^{(3)}$ points. The $L^{(1)}$-point gap $E_g^{(1)}$ is negligibly small due to the small value of $\alpha_{33}^{film}(Bi_{1-x}Sb_x)$, where a Dirac cone is formed, as shown in Fig. 4-1(a). However, the $L^{(2)}$- and $L^{(3)}$- point band gaps $E_g^{(2)}$ and $E_g^{(3)}$ are much larger, which implies that effectively a single-Dirac-cone at the $L^{(1)}$ point is constructed. Here we are taking advantage of both the extreme anisotropy of $Bi_{1-x}Sb_x$ and the quantum confinement effect of thin films. The quantum confinement effects for the $L^{(1)}$-point carriers differs remarkably from those for the $L^{(2)}$- and $L^{(3)}$-point carriers due to the anisotropy of the L-point pockets. Figure 4-1(b) shows that a $Bi_{1-x}Sb_x$ thin film grown along the binary axis can be a bi-Dirac-cone material, where the $L^{(1)}$-point band gap $E_g^{(1)}$ is much larger than the $L^{(2)}$- and $L^{(3)}$- point band gaps $E_g^{(2)}$ and $E_g^{(3)}$. Thus, $E_g^{(2)}$ and $E_g^{(3)}$ remain small enough to make two degenerate Dirac cones (quasi-Dirac cones) at the $L^{(2)}$ and the $L^{(3)}$ points. In Fig. 4-1(c), the film is grown along the trigonal axis, so

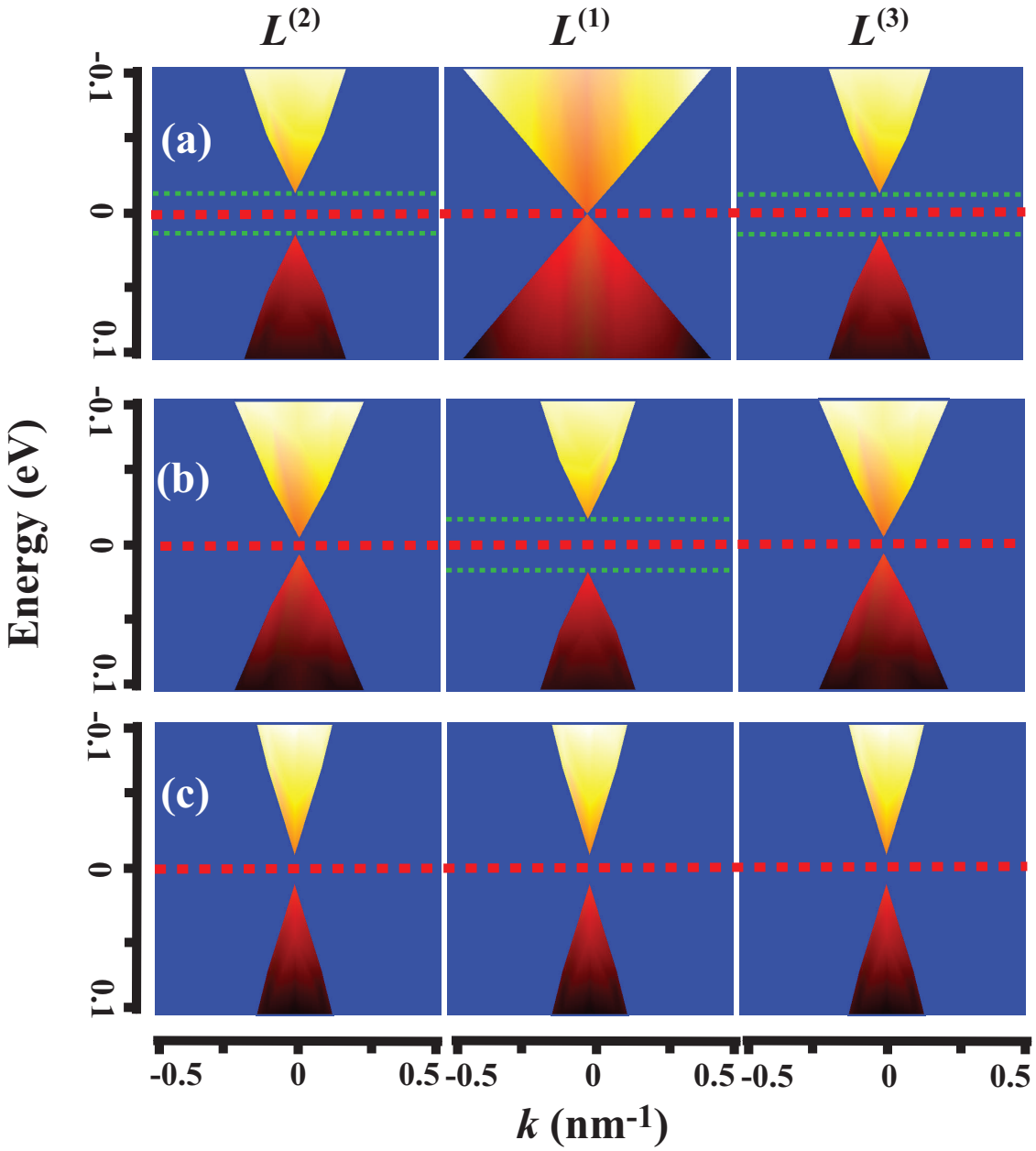

Figure 4-1: An illustration of (a) single-, (b) bi- and (c) tri-Dirac-cone $Bi_{1-x}Sb_x$ thin films grown along the (a) bisectrix, (b) binary and (c) trigonal axes, respectively. For the cross-sectional view of each cone, $\mathbf{k}$ is chosen such that $\nabla_{\mathbf{k}}E(\mathbf{k})$ has its minimum along that direction of $\mathbf{k}$. The illustration is based on the example of $Bi_{1-x}Sb_x$ thin films with $l_z = 100$ nm, $x = 0.04$, $P = 1$ atm and $T \leq 77$ K, under which the L points of bulk $Bi_{1-x}Sb_x$ have a zero-gap. The scenario is similar for other conditions. In (a), a single-Dirac-cone is formed at the $L^{(1)}$ point, while the $L^{(2)}$- and $L^{(3)}$- point band gaps are opened up. In (b), two degenerate quasi-Dirac cones are formed at the $L^{(2)}$ and $L^{(3)}$ points, while the $L^{(1)}$-point band gap is much larger, which leads to a bi-quasi-Dirac-cone material. The band gap at the $L^{(2)}$ and $L^{(3)}$ points can be less than 1 meV if a sample of $l_z = 200$ nm is chosen, which leads to exact Dirac cones for $L^{(1)}$. In (c), the $L^{(1)}$-, $L^{(2)}$- and $L^{(3)}$- point band gaps are all the same, and the three quasi-Dirac cones are degenerate in energy.

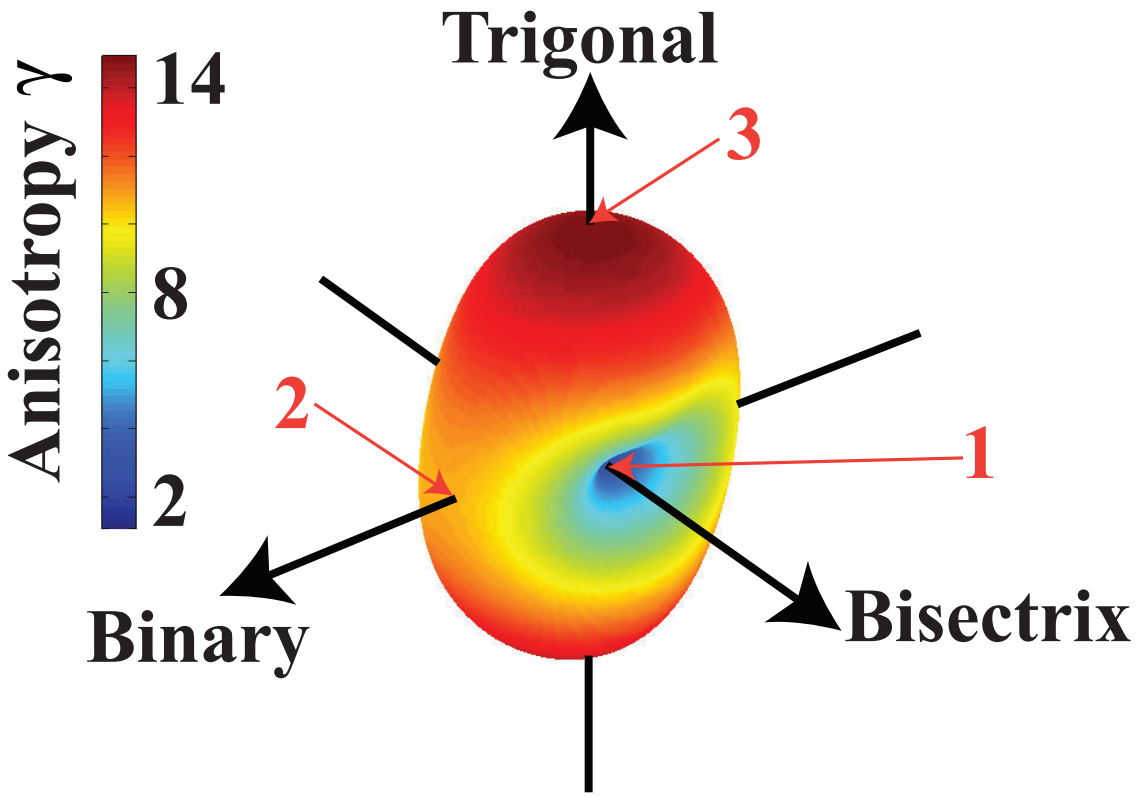

Figure 4-2: The anisotropy coefficient γ vs. film growth orientation. The value of γ for a specific film growth orientation is shown by the radius and the color, using the color scale on the left. γ can be as large as $\sim$14 for films grown along the trigonal axis, and as small as $\sim$2 for films grown along the bisectrix axis.

that the 3-fold symmetry for the three L points is retained. The three Dirac cones (quasi-Dirac cones) at the $L^{(1)}$, $L^{(2)}$ and $L^{(3)}$ points are degenerate in energy, which makes this film a tri-Dirac-cone material. By definition, an exact Dirac cone has $E_g = 0$. However, $E_g = 0$ Dirac cones are seldom achieved experimentally, so it is practical to consider $E_g \leq k_B T$ as a criterion for an exact Dirac cone. In the temperature range below 77 K that we are considering in this thesis, the thermal smearing of $k_B T$ corresponds to ~ 7 meV. For the criterion of a quasi-Dirac cone, we can use $k_B T \leq E_g \leq E_g(Bi)^{bulk}$, where $E_g(Bi)^{bulk} \simeq 14$ meV. Thus, we consider the three Dirac cones in Fig. 4-1(c), as quasi-Dirac cones, which are plotted for the case of $l_z = 100$ nm and $E_g \simeq 10$ meV. If exact Dirac cones are needed, a larger film thickness can be chosen, e.g. $l_z = 200$ nm, which satisfies $E_g \leq k_B T$.

We now show how to construct anisotropic Dirac cones with different shapes for the wave vector as a function of cone angle. To characterize the anisotropy of a Dirac cone, we

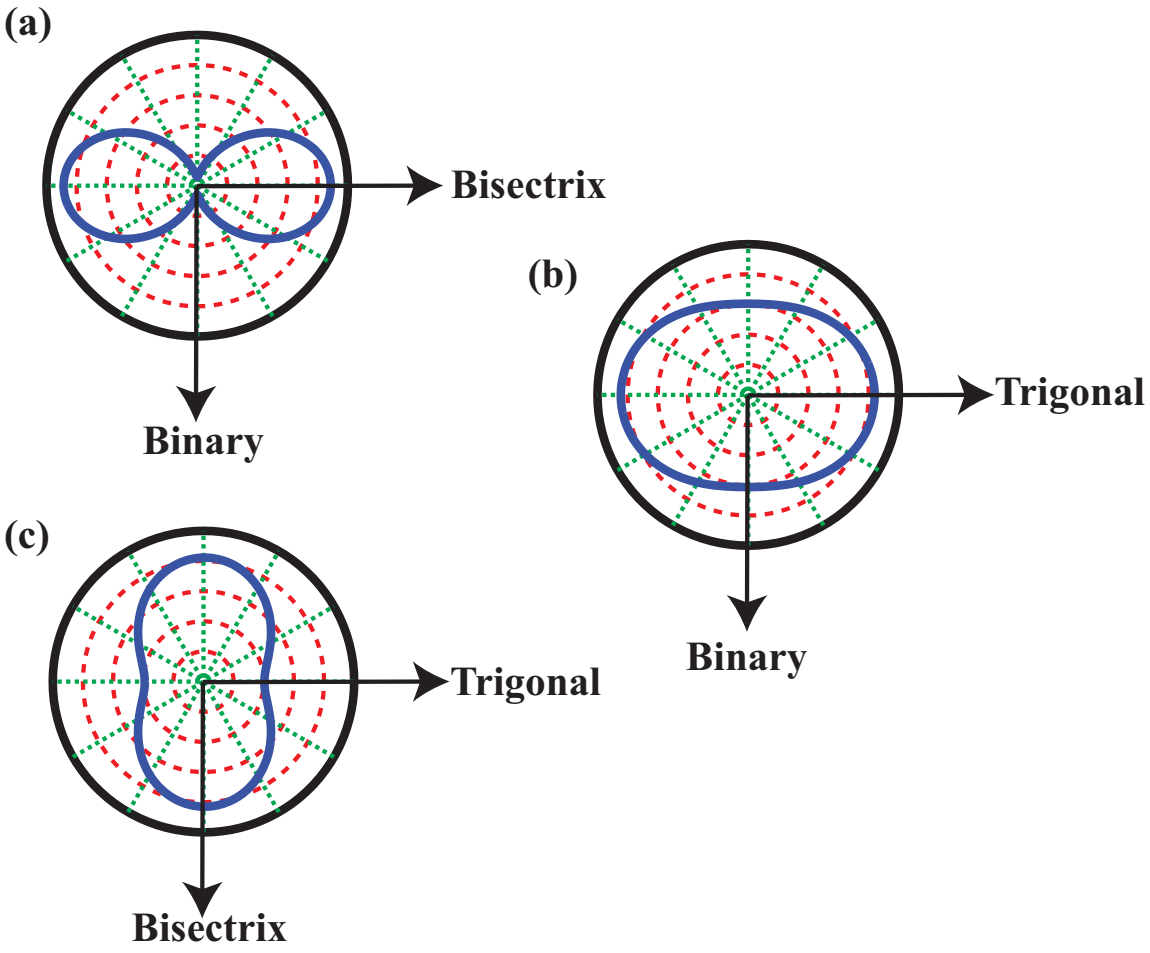

Figure 4-3: The velocity **v** is shown for the $L^{(1)}$-point Dirac fermions vs. transport direction for $Bi_{1-x}Sb_x$ thin films grown along the (b) trigonal, (c) bisectrix and (d) binary axes. (b)-(c) are drawn based on an example sample with $l_z = 300$ nm and $x = 0.04$.

define an anisotropy coefficient

$$\gamma = \frac{|\mathbf{v}_{\max}|}{|\mathbf{v}_{\min}|}, \tag{4.1}$$

where $\mathbf{v}_{\max}$ and $\mathbf{v}_{\min}$ are the maximum and minimum in-film carrier group velocities for a Dirac cone that is defined as $\mathbf{v}(\mathbf{k}) = \nabla_{\mathbf{k}} E(\mathbf{k})$. For a perfect Dirac cone, $\mathbf{v}$ is a function of the direction of the lattice momentum $\mathbf{k}$ measured from that L point only and is independent of the magnitude of $\mathbf{k}$. For an imperfect Dirac cone or a quasi-Dirac cone, this magnitude invariance is exact only when $\mathbf{k}$ is large, and becomes an approximation around the apex when $\mathbf{k}$ is small.

Figure 4-2 and 4-3 give us an important guide on how to construct anisotropic $L^{(1)}$-point Dirac cones. In Fig. 4-2, the anisotropy coefficient γ for the $L^{(1)}$-point Dirac cone as a function of film growth orientation is shown. For a film grown along the bisectrix axis, γ has its minimum value $\gamma_{min} = \sim 2$, where the carrier velocity $\mathbf{v}(\mathbf{k})$ for the $L^{(1)}$-point Dirac cone varies only by a small amount with the direction of $\mathbf{k}$, as shown in Fig. 4-3(a). For a film grown along the binary axis, $\gamma = \sim 10$, where $\mathbf{v}(\mathbf{k})$ varies more with the direction of $\mathbf{k}$ as shown in Fig. 4-3(b), compared to Fig. 4-3(a). For a film grown along the trigonal axis, γ has its maximum of $\gamma_{max} = \sim 14$, where $\mathbf{v}$ varies significantly with the direction of $\mathbf{k}$, as shown in Fig. 4-3(c).

Researchers have tried to realize semi-Dirac cones in oxide layers [83, 84], where the fermions are relativistic in one direction and classical in its orthogonal direction. In the present work, we have found that it is possible to construct semi-Dirac cones in the $Bi_{1-x}Sb_x$ thin film system. According to Eqs. 2.12 and 3.1, for an in-film direction $\hat{\mathbf{k}}$, where $\hat{\mathbf{k}}$ is a unit directional vector of $\mathbf{k}$ in the in-film lattice momentum space, whether the dispersion relation is linear or parabolic depends on the L-point band gap E_g, and the $\tilde{\boldsymbol{\alpha}}$ projection along that direction of $\hat{\mathbf{k}}$, defined by $\tilde{\alpha}_{\hat{\mathbf{k}}} = \hat{\mathbf{k}}^* \cdot \tilde{\boldsymbol{\alpha}} \cdot \hat{\mathbf{k}}$, where $\tilde{\boldsymbol{\alpha}}$ is given by Eq. (3.1). When E_g is small and $\tilde{\alpha}_{\hat{\mathbf{k}}}$ is large, the energy becomes linearly dispersed along $\hat{\mathbf{k}}$; when E_g is large and $\tilde{\alpha}_{\hat{\mathbf{k}}}$ is small, the energy becomes parabolically dispersed along $\hat{\mathbf{k}}$. To construct a semi-Dirac cone, we need to find a proper L-point band gap E_g and anisotropy γ, such that $E_g/\tilde{\alpha}_{\max}$ is small and $E_g/\alpha_{\min}$ is large. In this case, the electronic energy is linearly dispersed along the $\tilde{\alpha}_{\max}$ direction and parabolically dispersed along the $\alpha_{\min}$

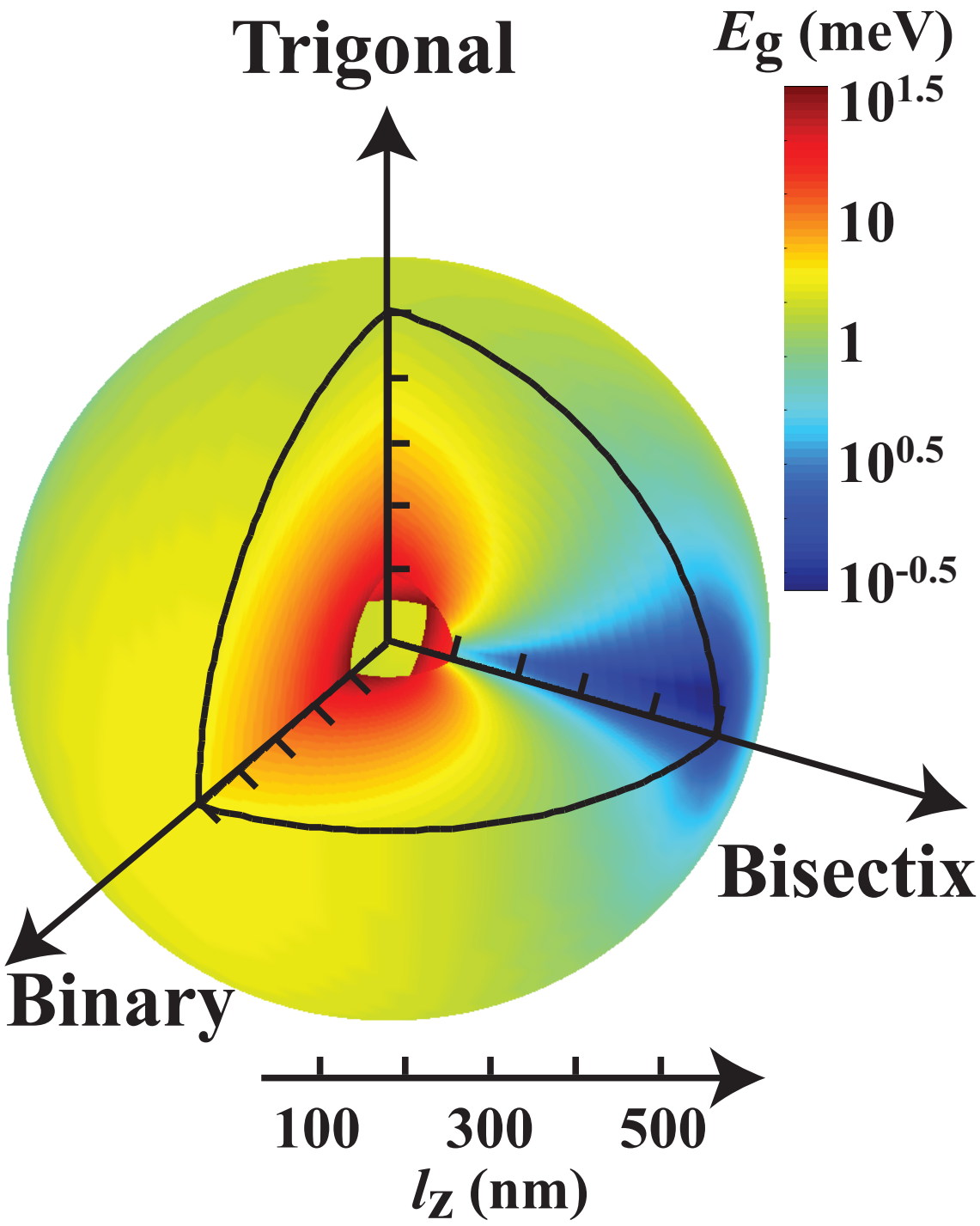

Figure 4-4: Illustration of a schematic view of the $L^{(1)}$-point band gap vs. film growth orientation and film thickness. The radius, the direction and the color represent the film thickness, the film growth orientation and the $L^{(1)}$-point band gap, respectively. The illustration takes $x = 0.04$ as an example. For other antimony compositions, film thickness and film growth orientation dependence for the $L^{(1)}$-point band gap should be similar, which is illustrated in Fig. 4-5.

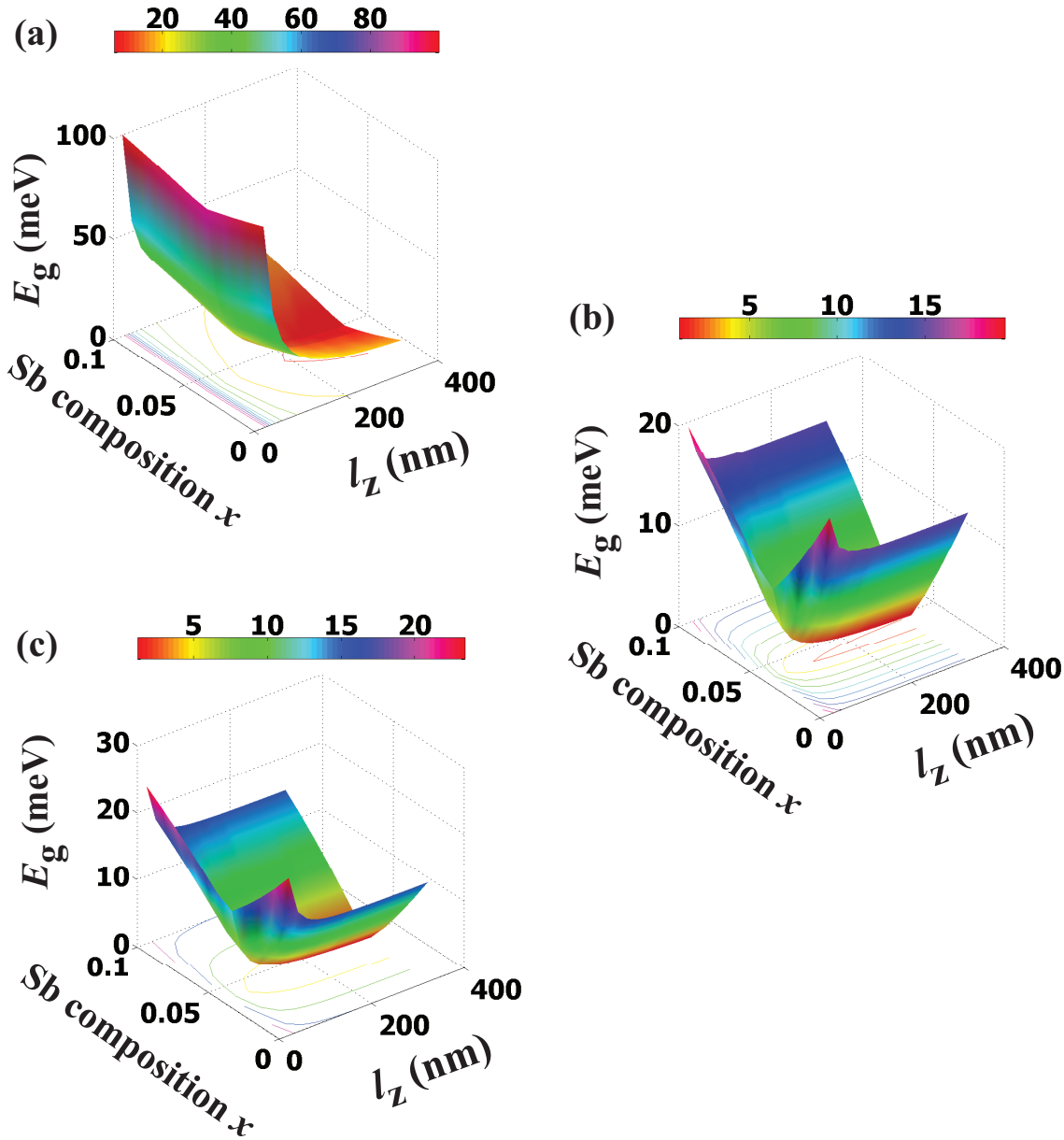

Figure 4-5: Schematic predictions of the $L^{(1)}$-point band gap vs. film thickness l_z and antimony composition x, for (a) trigonal direction growth, (b) bisectrix direction growth and (c) binary direction growth.

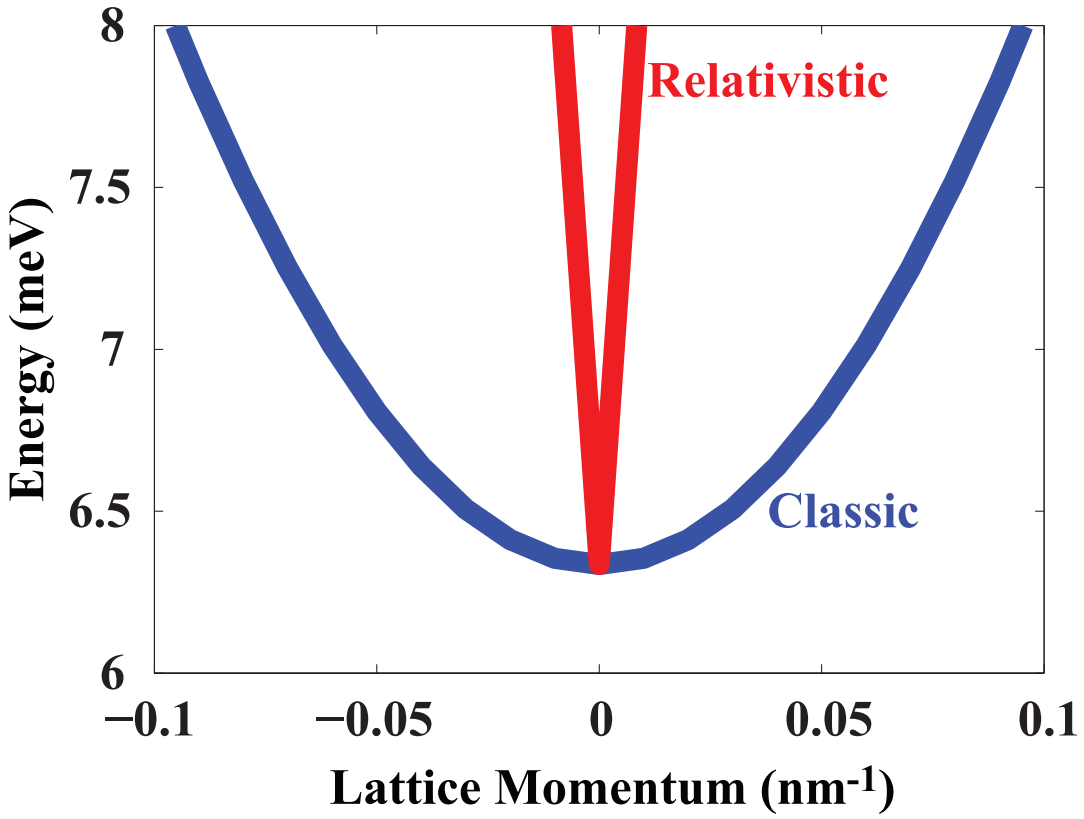

Figure 4-6: Example of a semi-Dirac cone in the $Bi_{1-x}Sb_x$ thin film system ($x = 0.10$ and $l_z = 100$ nm). It can be seen that around the $L^{(1)}$ point, the fermions are relativistic (linearly dispersed) along the $\mathbf{v}_{\text{max}}$ direction, and classical (parabolically dispersed) along the $\mathbf{v}_{\text{min}}$ direction.

direction. Here $\tilde{\alpha}_{\max}$ and $\tilde{\alpha}_{\min}$ are the maximum and minimum values of $\tilde{\alpha}_{\hat{\mathbf{k}}}$, which correspond to the principal axes of the 2D tensor $\tilde{\boldsymbol{\alpha}}$. The L-point band gap varies as a function of the film thickness l_z, the growth orientation and antimony composition x, as shown by the calculated results given in Fig. 4-4 and 4-5. To construct a semi-Dirac cone, we need to find a growth direction that ensures a significant anisotropy, and a large enough value of E_g which ensures that $E(\mathbf{k})$ becomes parabolically dispersed along the $\tilde{\alpha}_{\min}$ direction. However, the E_g should not be too large, because of the necessity that the linear dispersion relation along the $\tilde{\alpha}_{\max}$ direction is maintained. These requirements can all be achieved by choosing the proper antimony composition x, film thickness l_z and growth orientation as shown in Figs. 4-4 and 4-5. From Figs. 4-1, 4-2 and 4-3, we know that the $L^{(1)}$-point Dirac cone has a maximum $\mathbf{k}$-vector anisotropy, when the growth orientation is near the trigonal axis. We also see that the thin film becomes a single-Dirac-cone material when the growth direction is near the bisectrix axis. Thus, a good strategy to construct a semi-Dirac cone is to choose a growth orientation between the trigonal and the bisectrix axis, in the trigonal-bisectrix plane. An example of a semi-Dirac cone is shown in Fig. 4-6, where the example sample is grown along a direction that is 40° from the trigonal axis, 50° from the bisectrix axis, and perpendicular to the binary axis. Thus, a large antimony composition (e.g. $x \approx 0.10$) and a small film thickness (e.g. $l_z \approx 100$ nm) is preferred to make the E_g large, and $x = 0.10$ and $l_z = 100$ nm are chosen for this example sample.

4.3 Conclusion

In conclusion, we have proposed the growth of $Bi_{1-x}Sb_x$ thin films, which for selected concentrations of Sb and different directions to the film normal allows different Dirac-cone materials to be constructed. We have shown how to construct single-, bi- and tri-Dirac-cone materials, as shown in Fig. 4-1, as well as quasi- and semi-Dirac-cone materials, as shown in Fig. 4-1(c) and Fig. 4-6, respectively.

Chapter 5

Conclusions and Future Directions

5.1 Conclusions

In this thesis, an iterative-two-dimensional-two-band model for studying the electronic band structure of $Bi_{1-x}Sb_x$ thin films has been developed. Based on this iterative-two-dimensional-two-band model, we predict that a large variety of Dirac-cone materials can be constructed, including the anisotropic single-Dirac-cone materials with differet anisotropies, the bi-Dirac-cone materials, the tri-Dirac-cone materials, the quasi-Dirac-cone materials and the semi-Dirac-cone materials.

The iterative-two-dimensional-two-band model for $Bi_{1-x}Sb_x$ thin films starts from the basic Lax model for bulk bismuth. We have extended this model to describe a two-dimensional thin film system of $Bi_{1-x}Sb_x$. The L-point band gap and the inverse-effective-mass tensor are evaluated by utilizing the iteration techniques. We also have introduced the Euler-angle rotation system to describe a general growth orientation. This whole methodology can also be extended to study other two-dimensional narrow-band materials systems, where there are strongly coupled bands at the band edges and where the dispersion relations are non-parabolic or linear, for example, the X-point dispersion relation of $Si_{1-x}Ge_x$, the L-point dispersion relation of PbTe. By small modifications, this model can also be extended to describe other low-dimensional narrow-band systems, such as nanowires.

Based on the iterative-two-dimensional-two-band model we have developed, we have also studied how to construct anisotropic single-Dirac-cone materials. We have found that

by growing the $Bi_{1-x}Sb_x$ thin film normal to a low symmetry direction, we can have a single L-point that differs from the other two by breaking the 3-fold symmetry occurring in the three-dimensional case. The two quantities, the bulk-band-gap term $E_g^{bulk}(Bi_{1-x}Sb_x)$ and the quantum-confinement-induced term $h^2\alpha_{33}^{[0]}/4 \cdot l_z^2$ for this special single L-point are minimized. We have predicted how to construct anisotropic single-Dirac-cones with different anisotropies in the $Bi_{1-x}Sb_x$ thin film system using the same formulae.

We have also studied how to construct a large variety of Dirac-cone materials in the $Bi_{1-x}Sb_x$ thin film system, including bi-Dirac-cone materials, tri-Dirac-cone materials, quasi-Dirac-cone materials and semi-Dirac-cone materials.

The work in this thesis have been written up for publications [85, 86, 87]. The work has been supported by Solid State Solar Thermal Energy Conversion Center on room-temperature thermoelectrics of Energy Frontier Research Centers Program, U.S. Department of Energy and then Air Force Office of Scientific Research, MURI Grant on cryogenic-temperature thermoelectrics, because the $Bi_{1-x}Sb_x$ thin films materials system can be used best at cryogenic temperatures.

5.2 Suggestions for Future Studies

From the work we have done in this thesis, a lot of future studies could be potentially done. Firstly, the transport of $Bi_{1-x}Sb_x$ thin films with different antimony composition x, growth orientation and film thickness can be studied. The optimization condition where the figure of merit ZT for cryogenic thermoelectrics and cooling device design can now be studied.

Secondly, the study methodology we use in this thesis can be used to study other narrow-band thin films systems, for example the silicon-germanium alloys thin films, the lead telluride thin films.

Thirdly, the model can be extended to the one-dimensional system and $Bi_{1-x}Sb_x$ nanowires can be studied in a similar way. Levin et al [56] have already carried out some work on $Bi_{1-x}Sb_x$ nanowires using this model.

Bibliography

[1] B. Lenoir, M. Cassart, J. P. Michenaud, H. Scherrer, and S. Scherrer, Journal of Physics and Chemistry of Solids **57**, 89 (1996).

[2] S. Tanuma, Journal of the Physical Society of Japan **16**, 2354 (1961).

[3] H. Goldsmid, Physica Status Solidi (a) **1**, 7 (1970).

[4] N. A. Sidorenko, Cryogenics **32**, 40 (1992).

[5] S. Tanuma, Journal of the Physical Society of Japan **16**, 2349 (1961).

[6] S. Golin, Physical Review **176**, 830 (1968).

[7] N. Brandt, Y. Ponomarev, and S. Chudinov, Journal of Low Temperature Physics **8**, 369 (1972).

[8] N. Brandt, S. Chudinov, and V. Karavaev, Soviet Journal of Experimental and Theoretical Physics **34**, 368 (1972).

[9] E. J. Tichovolsky and J. G. Mavroides, Solid State Communications **7**, 927 (1969).

[10] H. Chu and Y. Kao, Physical Review B **1**, 2377 (1970).

[11] N. Brandt, E. Svistova, and M. Semenov, Soviet Journal of Experimental and Theoretical Physics **32**, 238 (1971).

[12] K. Hiruma, G. Kido, and N. Miura, Solid State Communications **38**, 859 (1981).

[13] A. Jain, Physical Review **114**, 1518 (1959).

[14] W. Kraak, Phys. Stat. Sol.(b) **88**, 105 (1978).

[15] B. Lenoir, A. Dauscher, M. Cassart, Y. Ravich, and H. Scherrer, Journal of Physics and Chemistry of Solids **59**, 129 (1998).

[16] E. Rogacheva, Journal of Physics and Chemistry of Solids **69**, 580 (2008).

[17] E. I. Rogacheva, A. A. Drozdova, O. N. Nashchekina, M. S. Dresselhaus, and G. Dresselhaus, Applied Physics Letters **94**, 202111 (2009).

[18] D. Hsieh et al., Nature **452**, 970 (2008).

[19] L. Li et al., Science **321**, 547 (2008).

[20] V. Gusynin, S. Sharapov, and J. Carbotte, Physical Review Letters **96**, 256802 (2006).

[21] C. Park, L. Yang, Y. Son, M. Cohen, and S. Louie, Nature Physics **4**, 213 (2008).

[22] P. Plochocka et al., Physical Review Letters **100**, 87401 (2008).

[23] I. Pletikosi et al., Physical Review Letters **102**, 56808 (2009).

[24] M. Sprinkle et al., Physical Review Letters **103**, 226803 (2009).

[25] H. Goldsmid, British Journal of Applied Physics **14**, 271 (1963).

[26] G. Smith and R. Wolfe, Journal of Applied Physics **33**, 841 (2009).

[27] L. Hicks and M. Dresselhaus, Physical Review B **47**, 12727 (1993).

[28] L. Hicks, T. Harman, X. Sun, and M. Dresselhaus, Physical Review B **53**, 10493 (1996).

[29] Y. Lin, S. Cronin, O. Rabin, J. Ying, and M. Dresselhaus, Applied Physics Letters **79**, 677 (2001).

[30] O. Rabin, Y. Lin, and M. Dresselhaus, Applied Physics Letters **79**, 81 (2001).

[31] Y. Lin, O. Rabin, S. Cronin, J. Ying, and M. Dresselhaus, Applied Physics Letters **81**, 2403 (2002).

[32] O. Rabin, *Bismuth Nanowire and Antidot Array Studies Motivated by Thermoelectrisity*, PhD thesis, Massachusettes Institute of Technology, 2004.

[33] Y. Lin, S. Cronin, J. Ying, M. Dresselhaus, and J. Heremans, Applied Physics Letters **76**, 3944 (2000).

[34] Y. Lin, X. Sun, and M. Dresselhaus, Physical Review B **62**, 4610 (2000).

[35] Z. Zhang, X. Sun, M. S. Dresselhaus, J. Y. Ying, and J. Heremans, Physical Review B **61**, 4850 (2000).

[36] B. Lax and J. Mavroides, *Solid State Physics*, volume 11, Academic Press, New York, 1960.

[37] B. Lax, J. G. Mavroides, H. J. Zeiger, and R. J. Keyes, Physical Review Letters **5**, 241 (1960).

[38] D. Schiferl and C. S. Barrett, Journal of Applied Crystallography **2**, 30 (1969).

[39] R. W. G. Wyckoff, *Crystal Structures*, Interscience, New York, 1964, Volume 1.

[40] PDF-2 Powder Diffraction File, JCPDS - The International Center for Diffraction Data.

[41] M. S. Dresselhaus, Electronic properties of the group v semimetals, in *Proceedings of the Conference on the Physics of Semimetals and Narrow Gap Semiconductors*, edited by D. L. Carter and R. T. Bate, pages 3–33, New York, NY, 1970, Pergamon Press.

[42] K. Bolotin et al., Solid State Communications **146**, 351 (2008).

[43] M. P. Vecchi and M. S. Dresselhaus, Physical Review B **10**, 771 (1974).

[44] M. Vecchi, J. Pereira, and M. Dresselhaus, Physical Review B **14**, 298 (1976).

[45] R. Isaacson and G. Williams, Physical Review **185**, 682 (1969).

[46] W. Datars and J. Vanderkooy, IBM Journal of Research and Development **8**, 247 (1964).

[47] R. Hartman, Physical Review **181**, 1070 (1969).

[48] M. H. Cohen and E. I. Blount, Philosophical Magazine **5**, 115 (1960).

[49] G. E. Smith, J. K. Galt, and F. R. Merritt, Phys. Rev. Lett. **4**, 276 (1960).

[50] R. N. Brown, J. G. Mavroides, and B. Lax, Phys. Rev. **129**, 2055 (1963).

[51] G. E. Smith, Phys. Rev. Lett. **9**, 487 (1962).

[52] R. Dinger and A. Lawson, Physical Review B **7**, 5215 (1973).

[53] F. Buot, Physical Review A **8**, 1570 (1973).

[54] D. Brust, Phys. Rev. **134**, A1337 (1964).

[55] J. O. Dimmock and G. B. Wright, Phys. Rev. **135**, A821 (1964).

[56] A. Levin and M. Dresselhaus, manuscript to be submitted.

[57] K. S. Novoselov et al., Nature **438**, 197 (2005).

[58] Y. Zhang, Y.-W. Tan, H. L. Stormer, and P. Kim, Nature **438**, 201 (2005).

[59] M. I. Katsnelson, K. S. Novoselov, and A. K. Geim, Nat Phys **2**, 620 (2006).

[60] S. Pathak, V. Shenoy, and G. Baskaran, Physical Review B **81**, 085431 (2010).

[61] J. Moore, Nature **464**, 194 (2010).

[62] J. Moore, Nature Physics **5**, 378 (2009).

[63] L. Fu and C. Kane, Physical Review Letters **100**, 96407 (2008).

[64] X. Qi, R. Li, J. Zang, and S. Zhang, Science **323**, 1184 (2009).

[65] J. Linder, Y. Tanaka, T. Yokoyama, A. Sudb, and N. Nagaosa, Physical Review Letters **104**, 67001 (2010).

[66] R. Shen, L. B. Shao, B. Wang, and D. Y. Xing, Physical Review B **81**, 041410 (2010).

[67] C.-H. Park, L. Yang, Y.-W. Son, M. L. Cohen, and S. G. Louie, Physical Review Letters **101**, 126804 (2008).

[68] P. Chao, H. Chu, and Y. Kao, Physical Review B **9**, 4030 (1974).

[69] J. A. van Hulst, H. M. Jaeger, and S. Radelaar, Physical Review B **52**, 5953 (1995).

[70] D. Morelli, D. Partin, and J. Heremans, Semiconductor Science and Technology **5**, S257 (1990).

[71] E. Rogacheva, D. S. Orlova, M. S. Dresselhaus, and S. Tang, Size effect in bi-sb solid solutions thin films, in *Materials Research Society Symposium Proceeding*, volume 1314, 2011.

[72] V. Sandomirskii, Soviet Journal of Experimental and Theoretical Physics **25**, 101 (1967).

[73] H. Asahi, T. Humoto, and A. Kawazu, Physical Review B **9**, 3347 (1974).

[74] L. Li, Y. Zhang, G. Li, and L. Zhang, Chemical Physics Letters **378**, 244 (2003).

[75] J. Heremans et al., Physical Review B **61**, 2921 (2000).

[76] L. Li, Y. Zhang, G. Li, X. Wang, and L. Zhang, Materials Letters **59**, 1223 (2005).

[77] J. Wang, X. Wang, Q. Peng, and Y. Li, Inorganic Chemistry **43**, 7552 (2004).

[78] C. G. Jin et al., Journal of Materials Chemistry **13**, 1743 (2003).

[79] Y. Cheng, A. Weiner, C. Wong, M. Balogh, and M. Lukitsch, Applied Physics Letters **81**, 3248 (2002).

[80] W. Shim, J. Ham, J. Kim, and W. Lee, Applied Physics Letters **95**, 232107 (2009).

[81] Y. Xu et al., Nanotechnology **19**, 115602 (2008).

[82] K. Novoselov et al., Science **306**, 666 (2004).

[83] S. Banerjee, R. R. P. Singh, V. Pardo, and W. E. Pickett, Physical Review Letters **103**, 016402 (2009).

[84] V. Pardo and W. E. Pickett, Physical Review Letters **102**, 166803 (2009).

[85] S. Tang and M. Dresselhaus, Arxiv preprint arXiv:1110.5391 (2011).

[86] S. Tang and M. Dresselhaus, Arxiv preprint arXiv:1111.5525 (2011).

[87] S. Tang and M. Dresselhaus, Bulletin of the American Physical Society (2012).